NEIGHBORING OPTIMAL GUIDANCE AND CONSTRAINED ATTITUDE CONTROL APPLIED TO THREE-DIMENSIONAL LUNAR ASCENT AND ORBIT INJECTION

Mauro Pontani
Department of Astronautical, Electrical, and Energy Engineering, Sapienza – University of Rome, Italy
mauro.pontani@uniroma1.it

Fabio Celani
School of Aerospace Engineering, Sapienza – University of Rome, Italy
fabio.celani@uniroma1.it

Future human or robotic missions to the Moon will require efficient ascent path and accurate orbit injection maneuvers, because the dynamical conditions at injection affect the subsequent phases of spaceflight. This research is focused on the original combination of two techniques applied to lunar ascent modules, i.e. (i) the recently-introduced variable-time-domain neighboring optimal guidance (VTD-NOG), and (ii) a constrained proportional-derivative (CPD) attitude control algorithm. VTD-NOG belongs to the class of implicit guidance approaches, aimed at finding the corrective control actions capable of maintaining the spacecraft sufficiently close to the reference trajectory. CPD pursues the desired attitude using thrust vector control and side jet system, while constraining the rates of both the thrust deflection angle and the roll control torque. After determining the optimal two-dimensional ascent path, which represents the reference trajectory, VTD-NOG & CPD is applied in the presence of nonnominal flight conditions, namely those due to navigation and actuation errors, incorrect initial position, unpredictable oscillations of the propulsive thrust, and imperfect modeling of the spacecraft mass distribution and variation. These stochastic deviations are simulated in the context of extensive Monte Carlo campaigns, and yield three-dimensional perturbed trajectories. The numerical results obtained in this work unequivocally demonstrate that VTD-NOG & CPD represents an accurate and effective methodology for guidance and control of lunar ascent path and orbit injection.

I. INTRODUCTION

Recently, several countries have shown an increasing interest toward robotic or human missions to the Moon. Ascent path and orbit injection represent a crucial issue for a lunar module, because the dynamical conditions at injection affect the subsequent phases of spaceflight.

In the scientific literature, only a limited number of works dealt with the joint application of guidance and control (G&C) algorithms to aerospace vehicles. In Ref. 1 proportional-derivative (PD) control is employed for both guidance and control algorithms. Guidance and control based on Nonlinear Dynamic Inversion is studied by Marcos et al.[2], and a comparison between Dynamic Inversion and State Dependent Riccati Equation approaches is presented in Ref. 3. An integrated G&C method is proposed by Tian et al.[4], while the use of G&C based on sliding-mode is investigated in Ref. 5.

This research is focused on the original combination of two techniques applied to lunar ascent modules, i.e. (i) the recently-introduced variable-time-domain neighboring optimal guidance (VTD-NOG), and (ii) a constrained proportional-derivative (CPD) attitude control algorithm. In particular, VTD-NOG is a special type of neighboring optimal guidance (NOG), and belongs to the class of feedback implicit guidance approaches[6-8], aimed at finding the corrective control actions capable of maintaining the spacecraft sufficiently close to the reference trajectory. This is an optimal path that satisfies the second-order sufficient conditions for optimality, similar to what occurs for alternative NOG schemes. Only a limited number of works have been devoted to studying NOG[9-14]. A common difficulty encountered in implementing the NOG consists in the fact that the gain matrices become singular while approaching the final time. A fundamental original feature of VTD-NOG is the use of a normalized time scale as the domain in which the nominal trajectory and the related vectors and matrices are defined. As a favorable consequence, the gain matrices remain finite for the entire time of flight. This leads also to obtaining new equations for the sweep method, which provides all the time-varying gain matrices, computed offline and stored in the onboard computer. In this mathematical framework, the updating formula for the time of flight and the guidance termination criterion are derived in a logical, consistent fashion. VTD-NOG identifies the trajectory corrections by assuming a thrust direction always aligned with the longitudinal axis of the spacecraft. However, this assumption represents an approximation, and the

attitude control system must be capable of maintaining the actual spacecraft orientation sufficiently close to this thrust alignment condition. To do this, the attitude control system uses thrust vector control (TVC) and side jet system (SJS). These techniques are widely employed for rocket and spacecraft attitude control[5,15]. PD control represents a consolidated approach to designing a closed-loop attitude control system[16]. However, plain PD control can lead to excessive rates for the control inputs. In fact, high proportional and derivative gains are often needed to obtain a fast response of the attitude control loop. Thus, in this work, attitude control is performed using CPD, which introduces an appropriate saturation action, with the final aim of maintaining the rates of the control inputs within acceptable limits. In particular, this study describes the application of VTD-NOG & CPD to lunar ascent. As a first step, the optimal two-dimensional trajectory is derived, and represents the nominal path. Then, the following perturbations are included in the dynamical modeling: (i) navigation errors, (ii) incorrect initial position, (iii) unpredictable oscillations of the propulsive thrust, (iv) actuation errors, and (v) imperfect modeling of the spacecraft mass distribution and variation. The resulting deviations from nominal flight conditions are evaluated, in the context of a Monte Carlo campaign. While the nominal path is two-dimensional, the perturbed trajectories are three-dimensional.

In Ref. 17 a similar guidance and control problem was studied. However, only perturbations on the propulsive thrust were considered. As a result, in that work only two-dimensional perturbed trajectories were investigated. Consequently, the translational and attitude dynamics, as well as the attitude control system employed in that paper, were significantly simpler than those considered in the present work. This research has thus the ultimate purpose of demonstrating that the joint use of VTD-NOG & CPD indeed represents an effective and accurate methodology for spacecraft guidance and control, with special reference to three-dimensional lunar ascent perturbed paths ending with accurate orbit injection. A preliminary version of this study can be found in Ref. 18.

II. LUNAR ASCENT PATH OPTIMIZATION

This paper addresses the problem of driving a spacecraft from the Moon surface to a final elliptic orbit, with specified periselenium and aposelenium altitudes (denoted respectively with h_P and h_A; $h_P = 15$ km and $h_A = 100$ km), in the presence of nonnominal flight conditions. Both trajectory and attitude dynamics of the space vehicle are modeled. This section is specifically devoted to defining the nominal ascent path. In this context, the space vehicle is modeled as a point mass. Subsequently, attitude dynamics is considered, with the final intent of determining the appropriate attitude control action.

The nominal vehicle ascent path is assumed to end at periselenium, and is investigated under the following three assumptions: (i) the Moon is spherical, as well as its mass distribution, (ii) the Moon does not rotate, and (iii) the spacecraft thrust is continuous and constant in magnitude. While (i) and (ii) are reasonable approximations, in consideration of the short time of flight, assumption (iii) leads to the following expression for the thrust acceleration $\left(T/\tilde{m}\right)$:

$$\frac{T}{\tilde{m}} = \frac{n_0 c}{c - n_0 t} \qquad [1]$$

where c is the (constant) effective exhaust velocity of the propulsive system, n_0 is the initial thrust acceleration (at t_0, set to 0), and t is the actual time. The following nominal values are assumed: $n_0 = 0.25 g_0$ and $c = 3$ km/sec $\left(g_0 = 9.8 \text{ m/sec}^2\right)$.

II.I Formulation of the problem

The spacecraft motion can be described in a convenient Moon-centered inertial reference frame, associated with the right-handed sequence of unit vectors $\left(\hat{c}_1, \hat{c}_2, \hat{c}_3\right)$, where $\left(\hat{c}_1, \hat{c}_2\right)$ identifies the plane of the desired orbit and $\hat{c}_3$ is aligned with the related angular momentum. At the initial time the ascent vehicle is assumed to be placed at P, belonging to the plane of the desired orbit (cf. Fig. I(a)). The time-varying spacecraft position can be identified by the following three variables: radius r, right ascension ξ, and declination ϕ, portrayed in Fig. I(a). The spacecraft velocity can be projected into the rotating frame $\left(\hat{r}, \hat{t}, \hat{n}\right)$, where $\hat{r}$ is aligned with the position vector $\boldsymbol{r}$ and $\hat{t}$ is parallel to the $\left(\hat{c}_1, \hat{c}_2\right)$-plane (and in the direction of the spacecraft motion, cf. Fig. I(a)). The related components are denoted with $\left(v_r, v_t, v_n\right)$ and termed respectively radial, transverse, and normal velocity component. The state vector $\boldsymbol{x}$ (with components denoted with x_k $\left(k = 1, \ldots, 6\right)$) of the spacecraft includes the variables associated with the position and velocity vectors and is given by

$$\boldsymbol{x} := \begin{bmatrix} r & \xi & \phi & v_r & v_t & v_n \end{bmatrix}^T \qquad [2]$$

For lunar ascent paths, the use of $\left(v_r, v_t, v_n\right)$ in place of velocity magnitude, flight path angle, and heading angle, allows avoiding the singularity in the equations of motion at the initial time, when the spacecraft velocity is zero. The ascent vehicle is controlled through the thrust direction, defined by the in-plane angle α

and the out-of-plane angle β, both illustrated in Fig. I(b) (in which $\hat{T}$ is aligned with the thrust direction). Thus, the control vector $\boldsymbol{u}$ is

$$\boldsymbol{u} := \begin{bmatrix} u_1 & u_2 \end{bmatrix}^T = \begin{bmatrix} \alpha & \beta \end{bmatrix}^T \quad [3]$$

The equations of motion, also termed state equations, govern the spacecraft dynamics, and involve the state vector $\boldsymbol{x}$ and the control vector $\boldsymbol{u}$,

$$\dot{r} = v_r \quad [4]$$

$$\dot{\xi} = \frac{v_t}{r\cos\phi} \quad [5]$$

$$\dot{\phi} = \frac{v_n}{r} \quad [6]$$

$$\dot{v}_r = -\frac{\mu}{r^2} + \frac{v_t^2 + v_n^2}{r} + \frac{T}{\tilde{m}}\sin\alpha\cos\beta \quad [7]$$

$$\dot{v}_t = \frac{v_t}{r}\left(v_n\tan\phi - v_r\right) + \frac{T}{\tilde{m}}\cos\alpha\cos\beta \quad [8]$$

$$\dot{v}_n = -\frac{v_t^2}{r}\tan\phi - \frac{v_r v_n}{r} + \frac{T}{\tilde{m}}\sin\beta \quad [9]$$

where $\left(T/\tilde{m}\right)$ is given by Eq. [1] and $\mu\ \left(=4902.9\ \text{km}^3/\text{sec}^2\right)$ is the Moon gravitational parameter. Equations [4]-[9] are derived in Appendix A, and can be written in the general compact form

$$\dot{\boldsymbol{x}} = \tilde{\boldsymbol{f}}\left(\boldsymbol{x},\boldsymbol{u},t\right) \quad [10]$$

Due to the definition of the inertial frame in relation to the initial spacecraft position, the initial conditions (denoted with the subscript "0") are

$$\begin{aligned} r_0 &= R_M \quad \xi_0 = 0 \quad \phi_0 = 0 \\ v_{r0} &= 0 \quad v_{t0} = 0 \quad v_{n0} = 0 \end{aligned} \quad [11]$$

where $R_M\ \left(=1738\ \text{km}\right)$ is the Moon radius. The final conditions (denoted with the subscript "f ") at orbit injection are

$$\begin{aligned} r_f &= R_M + h_P \quad \phi_f = 0 \\ v_{rf} &= 0 \quad v_{tf} = \sqrt{\frac{\mu_M}{a}\frac{1+e}{1-e}} \quad v_{nf} = 0 \end{aligned} \quad [12]$$

where a and e represent respectively the semimajor axis and eccentricity of the desired orbit. Equations [11]-[12] can be written in compact form as

$$\boldsymbol{\psi}\left(\boldsymbol{x}_0,\boldsymbol{x}_f,t_f\right) = \boldsymbol{0} \quad [13]$$

The problem at hand can be reformulated by using the dimensionless normalized time τ,

$$\tau := t/t_f \quad \Rightarrow \quad \tau_0 \equiv 0 \le \tau \le 1 \equiv \tau_f \quad [14]$$

Let the dot denote the derivative with respect to τ. Equations [10] are rewritten as

$$\dot{\boldsymbol{x}} = t_f\tilde{\boldsymbol{f}}\left(\boldsymbol{x},\boldsymbol{u},t_f\tau\right) =: \boldsymbol{f}\left(\boldsymbol{x},\boldsymbol{u},\boldsymbol{a},\tau\right) \quad [15]$$

where $\boldsymbol{a}$ collects all the unknown parameters of the problem ($\boldsymbol{a} = t_f$ for the problem at hand).

Due to assumption (iii), minimizing the propellant consumption is equivalent to minimizing the time of flight $\left(t_f - t_0\right)$. Thus, as t_0 is set to 0, the objective function is

$$J = t_f \quad [16]$$

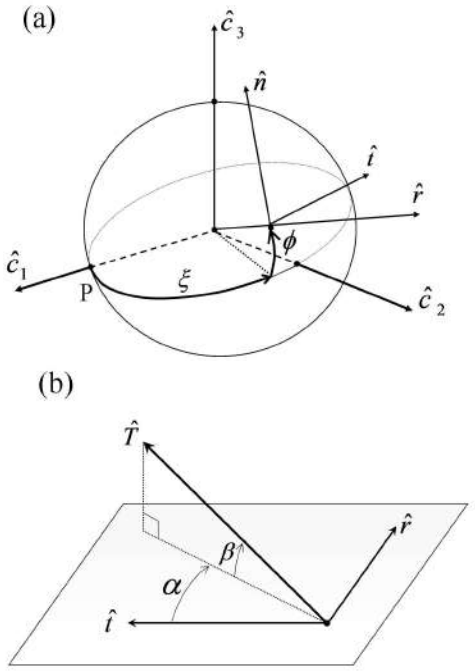

Fig. I: Reference frames (a) and thrust angles (b)

II.II First-order necessary conditions for an extremal

With the intent of obtaining the necessary conditions for a local extremal, the Hamiltonian H and the function of the boundary conditions $\tilde{\Phi}$ are introduced:

$$\begin{aligned} H\left(\boldsymbol{x},\boldsymbol{u},\boldsymbol{a}\right) &:= \boldsymbol{\lambda}^T\boldsymbol{f} = \lambda_1 t_f x_4 + \lambda_2\frac{t_f x_5}{x_1\cos x_3} + \lambda_3\frac{t_f x_6}{x_1} \\ &+ \lambda_4 t_f\left[-\frac{\mu}{x_1^2} + \frac{x_5^2 + x_6^2}{x_1} + \frac{T}{\tilde{m}}\sin u_1\cos u_2\right] \\ &+ \lambda_5 t_f\left[\frac{x_5}{x_1}\left(x_6\tan x_3 - x_4\right) + \frac{T}{\tilde{m}}\cos u_1\cos u_2\right] \\ &+ \lambda_6 t_f\left[\frac{x_5^2}{x_1}\tan x_3 - \frac{x_4 x_6}{x_1} + \frac{T}{\tilde{m}}\sin u_2\right] \end{aligned} \quad [17]$$

$$\begin{aligned} \tilde{\Phi}\left(\boldsymbol{x}_0,\boldsymbol{x}_f,\boldsymbol{a}\right) &:= t_f + \boldsymbol{\upsilon}^T\boldsymbol{\psi} = t_f + \upsilon_1\left(x_{10} - R_M\right) \\ &+ \upsilon_2 x_{20} + \upsilon_3 x_{30} + \upsilon_4 x_{40} + \upsilon_5 x_{50} + \upsilon_6 x_{60} \\ &+ \upsilon_7\left(x_{1f} - R_M - h_P\right) + \upsilon_9 x_{3f} + \upsilon_9 x_{4f} \\ &+ \upsilon_{10}\left[x_{5f} - \sqrt{\frac{\mu}{a}\frac{1+e}{1-e}}\right] + \upsilon_{11} x_{6f} \end{aligned} \quad [18]$$

where $x_{k0} = x_k(t_0)$ and $x_{kf} = x_k(t_f)$ $(k = 1,\ldots,6)$; λ and υ represent respectively the adjoint variable conjugate to the dynamics equations [15] and to the boundary conditions [13], with components $\{\lambda_j\}_{j=1,\ldots,6}$ and $\{\upsilon_j\}_{j=1,\ldots,11}$. The first-order necessary conditions for (local) optimality include the adjoint (or costate) equations[13], in conjunction with the related boundary conditons:

$$\dot{\boldsymbol{\lambda}} = -\left[\frac{\partial H}{\partial \boldsymbol{x}}\right]^T \qquad \boldsymbol{\lambda}_0 = -\left[\frac{\partial \tilde{\Phi}}{\partial \boldsymbol{x}_0}\right]^T \qquad \boldsymbol{\lambda}_f = \left[\frac{\partial \tilde{\Phi}}{\partial \boldsymbol{x}_f}\right]^T \quad [19]$$

The optimal control $\boldsymbol{u}^*$ can be expressed as a function of the costates through the Pontryagin minimum principle,

$$\boldsymbol{u}^* = \arg\min_{\boldsymbol{u}} \left[\lambda_4 \sin u_1 \cos u_2 + \lambda_5 \cos u_1 \cos u_2 + \lambda_6 \sin u_2\right] \quad [20]$$

leading to

$$\beta^* = -\arcsin \frac{\lambda_6^*}{\sqrt{\lambda_4^{*2} + \lambda_5^{*2} + \lambda_6^{*2}}} \quad [21]$$

$$\sin\alpha^* = -\frac{\lambda_4^*}{\sqrt{\lambda_4^{*2} + \lambda_5^{*2}}} \qquad \cos\alpha^* = -\frac{\lambda_5^*}{\sqrt{\lambda_4^{*2} + \lambda_5^{*2}}} \quad [22]$$

where the superscript "*" denotes the optimal value of the respective variable. Equations [21]-[22] imply the fulfillment of the stationarity condition of H with respect to $\boldsymbol{u}$. Lastly, the parameter condition[13] must hold, and yields

$$\int_0^1 \left[\frac{\partial H}{\partial \boldsymbol{a}}\right]^T d\tau + \left[\frac{\partial \tilde{\Phi}}{\partial \boldsymbol{a}}\right]^T = 0 \quad \Rightarrow \quad \int_0^1 \boldsymbol{\lambda}^T \frac{\partial \boldsymbol{f}}{\partial t_f} d\tau + 1 = 0 \quad [23]$$

After introducing the additional variable $\boldsymbol{\mu}$, Eq. [23] is equivalent to

$$\dot{\boldsymbol{\mu}} = -\left[\frac{\partial H}{\partial \boldsymbol{a}}\right]^T \quad \text{with} \quad \boldsymbol{\mu}_0 = 0 \quad \text{and} \quad \boldsymbol{\mu}_f - \left[\frac{\partial \tilde{\Phi}}{\partial \boldsymbol{a}}\right]^T = 0 \quad [24]$$

However, the parameter condition can be transformed into an inequality constraint, as a consequence of homogeneity of the costate equations, in conjunction with Eqs. [21]-[22], in which the control angles are expressed as the ratios of adjoint variables. In fact, due to Eqs. [21]-[22], homogeneity implies that if $\boldsymbol{\lambda}$ is proportional to $\boldsymbol{\lambda}^*$ ($\boldsymbol{\lambda} = k_\lambda \boldsymbol{\lambda}^*$; k_λ denotes a positive constant), then the final conditions are fulfilled at the minimum final time t_f^*. In contrast, the parameter condition is violated, because the integral of Eq. [23] turns out to be

$$\int_0^1 \boldsymbol{\lambda}^T \frac{\partial \boldsymbol{f}}{\partial t_f} d\tau = k_\lambda \int_0^1 \boldsymbol{\lambda}^{*T} \frac{\partial \boldsymbol{f}}{\partial t_f} d\tau = -k_\lambda \neq -1 \quad [25]$$

Therefore, provided that the proportionality condition holds, the optimal control $\boldsymbol{u}^*$ can be determined without considering the parameter condition, which can be replaced by the inequality constraint

$$\int_0^1 \boldsymbol{\lambda}^T \frac{\partial \boldsymbol{f}}{\partial t_f} d\tau < 0 \quad [26]$$

In the formulation of the problem the Moon is assumed spherical, as is its gravitational field. As no further external force affects the spacecraft motion the optimal ascent path can be assumed to lie entirely on the $(\hat{c}_1, \hat{c}_2)$-plane. The optimal planar trajectory can be reasonably conjectured to outperform any hypothetical alternative three-dimensional trajectory. In fact, due to symmetry of the gravitational field, any out-of-plane thrust maneuver has the effect of only rotating the instantaneous velocity and would imply a useless waste of propellant. In light of these considerations, the problem of determining the minimum-fuel path can be simplified by assuming that at any time the out-of-plane variables equal 0, i.e.

$$\phi = 0 \quad \text{and} \quad v_n = 0 \quad [27]$$

$$\lambda_3^* = 0 \quad \text{and} \quad \lambda_6^* = 0 \quad \Rightarrow \quad \beta^* = 0 \quad [28]$$

Only the state equations [4], [5], [7], and [8], the respective adjoint equations, and Eq. [22] are needed for the purpose of determining the optimal planar ascent path. The remaining adjoint equations, together with the related boundary conditions are identically satisfied if Eqs. [27]-[28] hold. In addition, Eq. [5] is ignorable, because no final condition is prescribed for the right ascension x_2, and x_2 does not appear in the right-hand-side of any state equation. This circumstance implies also that $\lambda_2 = 0 \ \forall \tau$. In the end, the optimal ascent path optimization problem can be formulated as a two-point boundary-value problem in which the unknowns are the initial values of the adjoint variables λ_1, λ_4, and λ_5, as well as the time of flight t_f. The final conditions to satisfy are those regarding r_f, v_{rf}, v_{tf} (cf. Eq. [12]), in conjunction with the inequality constraint [26].

II.III Second-order sufficient conditions for a minimum

The derivation of the second-order optimality conditions involves the definition of an admissible comparison path, located in the neighborhood of the (local) optimal path, associated with the state $\boldsymbol{x}^*$, costate $\boldsymbol{\lambda}^*$, and control $\boldsymbol{u}^*$. By definition, an admissible comparison path is a feasible trajectory that satisfies the equations of motion and the boundary conditions. The nonexistence of alternative neighboring optimal solutions is to be proven in order to guarantee optimality of the solution of interest[13].

The first second-order condition is the *Clebsch-Legendre sufficient condition* for a minimum[13], i.e. $H_{uu}^* > 0$. In the necessary (weak) form the sign "$\geq$"

replaces the inequality sign (i.e. the Hessian must be positive semidefinite).

In general, a comparison path fulfills the state equations and boundary conditions to first order. This means that the state and costate displacements $(\delta \boldsymbol{x}, \delta \boldsymbol{\lambda})$ satisfy the linear equations deriving from Eqs. [15] and [19],

$$\delta \boldsymbol{\lambda}_f - \Phi_{\boldsymbol{x}_f \boldsymbol{x}_f} \delta \boldsymbol{x}_f - \boldsymbol{\psi}_{\boldsymbol{x}_f}^T \delta \boldsymbol{\upsilon} - \Phi_{\boldsymbol{x}_f \boldsymbol{a}} d\boldsymbol{a} = \mathbf{0} \quad [29]$$

$$\delta \boldsymbol{\psi} = \boldsymbol{\psi}_{\boldsymbol{x}_f} \delta \boldsymbol{x}_f + \boldsymbol{\psi}_{\boldsymbol{a}} d\boldsymbol{a} = \mathbf{0} \quad [30]$$

Moreover, the fact that the Hamiltonian is stationary with respect to $\boldsymbol{u}$, i.e. $H_{\boldsymbol{u}}^* = \mathbf{0}^T$, yields

$$H_{\boldsymbol{u}\boldsymbol{x}} \delta \boldsymbol{x} + H_{\boldsymbol{u}\boldsymbol{u}} \delta \boldsymbol{u} + H_{\boldsymbol{u}\boldsymbol{a}} d\boldsymbol{a} + H_{\boldsymbol{u}\boldsymbol{\lambda}} \delta \boldsymbol{\lambda} = \mathbf{0} \quad [31]$$

The corresponding linear boundary conditions are derived from Eqs. [13] and [19][13]. The parameter condition [23] is replaced by Eq. [24], yielding the following relations:

$$\delta \dot{\boldsymbol{\mu}} = -H_{\boldsymbol{a}\boldsymbol{x}} \delta \boldsymbol{x} - H_{\boldsymbol{a}\boldsymbol{u}} \delta \boldsymbol{u} - H_{\boldsymbol{a}\boldsymbol{a}} \delta \boldsymbol{a} - H_{\boldsymbol{a}\boldsymbol{\lambda}} \delta \boldsymbol{\lambda} \quad [32]$$

with

$$\delta \boldsymbol{\mu}_0 = \mathbf{0}, \quad \delta \boldsymbol{\mu}_f - \tilde{\Phi}_{\boldsymbol{a}\boldsymbol{x}_f} \delta \boldsymbol{x}_f - \tilde{\Phi}_{\boldsymbol{a}\boldsymbol{a}} \delta \boldsymbol{a}^T - \boldsymbol{\psi}_{\boldsymbol{a}}^T d\boldsymbol{\upsilon} = \mathbf{0} \quad [33]$$

where Eq. [33] is written under the assumption that $\tilde{\Phi}_{\boldsymbol{a}\boldsymbol{x}_0} = 0$, condition that is met for the problems at hand. Under the assumption that the Clebsch-Legendre condition is satisfied, Eq. [31] can be solved for $\delta \boldsymbol{u}$:

$$\delta \boldsymbol{u} = -H_{\boldsymbol{u}\boldsymbol{u}}^{-1} \left(H_{\boldsymbol{u}\boldsymbol{x}} \delta \boldsymbol{x} + H_{\boldsymbol{u}\boldsymbol{a}} d\boldsymbol{a} + H_{\boldsymbol{u}\boldsymbol{\lambda}} \delta \boldsymbol{\lambda} \right) \quad [34]$$

After inserting the latter expression in the linear differential equations (for the state and the costate) as well as in Eq. [32], one obtains[13]

$$\delta \dot{\boldsymbol{x}} = \mathbf{A} \delta \boldsymbol{x} - \mathbf{B} \delta \boldsymbol{\lambda} + \mathbf{D} d\boldsymbol{a} \quad [35]$$

$$\delta \dot{\boldsymbol{\lambda}} = -\mathbf{C} \delta \boldsymbol{x} - \mathbf{A}^T \delta \boldsymbol{\lambda} - \mathbf{E} d\boldsymbol{a} \quad [36]$$

$$\delta \dot{\boldsymbol{\mu}} = -\mathbf{E}^T \delta \boldsymbol{x} - \mathbf{D}^T \delta \boldsymbol{\lambda} - \mathbf{F} d\boldsymbol{a} \quad [37]$$

where

$$\mathbf{A} = \boldsymbol{f}_{\boldsymbol{x}} - \boldsymbol{f}_{\boldsymbol{u}} H_{\boldsymbol{u}\boldsymbol{u}}^{-1} H_{\boldsymbol{u}\boldsymbol{x}} \quad [38]$$

$$\mathbf{B} = \boldsymbol{f}_{\boldsymbol{u}} H_{\boldsymbol{u}\boldsymbol{u}}^{-1} \boldsymbol{f}_{\boldsymbol{u}}^T \quad [39]$$

$$\mathbf{C} = H_{\boldsymbol{x}\boldsymbol{x}} - H_{\boldsymbol{x}\boldsymbol{u}} H_{\boldsymbol{u}\boldsymbol{u}}^{-1} H_{\boldsymbol{u}\boldsymbol{x}} \quad [40]$$

$$\mathbf{D} = \boldsymbol{f}_{\boldsymbol{a}} - \boldsymbol{f}_{\boldsymbol{u}} H_{\boldsymbol{u}\boldsymbol{u}}^{-1} H_{\boldsymbol{u}\boldsymbol{a}} \quad [41]$$

$$\mathbf{E} = H_{\boldsymbol{x}\boldsymbol{a}} - H_{\boldsymbol{x}\boldsymbol{u}} H_{\boldsymbol{u}\boldsymbol{u}}^{-1} H_{\boldsymbol{u}\boldsymbol{a}} \quad [42]$$

$$\mathbf{F} = H_{\boldsymbol{a}\boldsymbol{a}} - H_{\boldsymbol{a}\boldsymbol{u}} H_{\boldsymbol{u}\boldsymbol{u}}^{-1} H_{\boldsymbol{u}\boldsymbol{a}} \quad [43]$$

Equations [29], [30], and [33] justify the introduction of the sweep variables, through the following relations:

$$\delta \boldsymbol{\lambda} = \mathbf{S} \delta \boldsymbol{x} + \mathbf{R} d\boldsymbol{\upsilon} + \mathbf{m} d\boldsymbol{a} \quad [44]$$

$$\mathbf{0} = \mathbf{R}^T \delta \boldsymbol{x} + \mathbf{Q} d\boldsymbol{\upsilon} + \mathbf{n} d\boldsymbol{a} \quad [45]$$

$$\delta \boldsymbol{\mu} = \mathbf{m}^T \delta \boldsymbol{x} + \mathbf{n}^T d\boldsymbol{\upsilon} + \boldsymbol{\alpha} d\boldsymbol{a} \quad [46]$$

The sweep (differential) equations can be proven to hold[13] for **S**, **R**, **m**, **Q**, **n**, and $\boldsymbol{\alpha}$,

$$\dot{\mathbf{S}} = -\mathbf{C} - \mathbf{A}^T \mathbf{S} - \mathbf{S}\mathbf{A} + \mathbf{S}\mathbf{B}\mathbf{S} \quad [47]$$

$$\dot{\mathbf{R}} = \left(\mathbf{S}\mathbf{B} - \mathbf{A}^T \right) \mathbf{R} \quad [48]$$

$$\dot{\mathbf{m}} = \left(\mathbf{S}\mathbf{B} - \mathbf{A}^T \right) \mathbf{m} - \mathbf{S}\mathbf{D} - \mathbf{E} \quad [49]$$

$$\dot{\mathbf{Q}} = \mathbf{R}^T \mathbf{B} \mathbf{R} \quad [50]$$

$$\dot{\mathbf{n}} = \mathbf{R}^T \left(\mathbf{B}\mathbf{m} - \mathbf{D} \right) \quad [51]$$

$$\dot{\boldsymbol{\alpha}} = \mathbf{m}^T \left(\mathbf{B}\mathbf{m} - \mathbf{D} \right) - \mathbf{D}^T \mathbf{m} - \mathbf{F} \quad [52]$$

The respective boundary conditions are such that Eqs. [44]-[46] reduce to Eqs. [29], [30], and [33] at the final time, and this occurs if

$$\mathbf{S}_f = \Phi_{\boldsymbol{x}_f \boldsymbol{x}_f} \quad \mathbf{R}_f = \boldsymbol{\psi}_{\boldsymbol{x}_f}^T \quad \mathbf{m}_f = \Phi_{\boldsymbol{x}_f \boldsymbol{a}} \quad [53]$$

$$\mathbf{Q}_f = \mathbf{0}_{q \times q} \quad \mathbf{n}_f = \boldsymbol{\psi}_{\boldsymbol{a}} \quad \boldsymbol{\alpha}_f = \Phi_{\boldsymbol{a}\boldsymbol{a}} \quad [54]$$

The differentials $d\boldsymbol{\upsilon}$ and $d\boldsymbol{a}$ can be found simultaneously at τ_0 (at which $\delta \boldsymbol{\mu}_0 = \mathbf{0}$, cf. Eq. [33]), using Eqs. [45]-[46], leading to

$$\begin{bmatrix} d\boldsymbol{\upsilon} \\ d\boldsymbol{a} \end{bmatrix} = -\mathbf{V}_0^{-1} \mathbf{U}_0^T \delta \boldsymbol{x}_0 \quad [55]$$

where

$$\mathbf{U} := \begin{bmatrix} \mathbf{R} & \mathbf{m} \end{bmatrix} \text{ and } \mathbf{V} := \begin{bmatrix} \mathbf{Q} & \mathbf{n} \\ \mathbf{n}^T & \boldsymbol{\alpha} \end{bmatrix} \quad [56]$$

If Eq. [55] is used at τ_0, then $\delta \boldsymbol{\lambda}_0 = \left(\mathbf{S}_0 - \mathbf{U}_0 \mathbf{V}_0^{-1} \mathbf{U}_0^T \right) \delta \boldsymbol{x}_0$. Letting $\hat{\mathbf{S}} := \mathbf{S} - \mathbf{U}\mathbf{V}^{-1}\mathbf{U}^T$, it is relatively straightforward to demonstrate that the same sweep equation that holds for **S** must be satisfied also by $\hat{\mathbf{s}}$ (with $\hat{\mathbf{s}}$ in place of **S**), with boundary condition $\hat{\mathbf{S}} \to \infty$ as $\tau \to \tau_f \ (=1)$. From the previous relation on $\delta \boldsymbol{\lambda}_0$ and $\delta \boldsymbol{x}_0$ one can conclude that $\delta \boldsymbol{\lambda}_0 \to \mathbf{0}$ as $\delta \boldsymbol{x}_0 \to \mathbf{0}$, unless $\hat{\mathbf{s}}$ tends to infinity at an internal time $\bar{\tau}$ $\left(\tau_0 \le \bar{\tau} < \tau_f \right)$, which is referred to as *conjugate point*. If $\delta \boldsymbol{\lambda}_0 \to \mathbf{0}$ and $\delta \boldsymbol{x}_0 \to \mathbf{0}$ then also $\delta \boldsymbol{u} \to \mathbf{0}$. In the end, if $\hat{\mathbf{S}} < \infty \ \ \forall \tau \in \left[\tau_0, \tau_f \right[$ then no conjugate point exists and, as a result, no neighboring optimal path exists. This condition is also referred to as *Jacobi condition*.

Finally, it is worth remarking that, with the exception of the displacements $\left(\delta \boldsymbol{x}, \delta \boldsymbol{u}, \delta \boldsymbol{a}, \delta \boldsymbol{\lambda}, \delta \boldsymbol{\mu} \right)$, all the vectors and matrices reported in this section are evaluated along the nominal, optimal trajectory.

III.IV Optimal ascent trajectory

This subsection addresses the numerical determination of the minimum-time ascent path leading to injection into the desired lunar orbit. To this end, the first-order conditions for optimality are used, in conjunction with a simple implementation of particle swarm algorithm[19] (PSO). This is a heuristic optimization technique, based on the use of a population of individuals (or particles). Selection of the globally optimal parameters is the result of a number of iterations, in which the individuals share their information. This optimization approach is extremely intuitive and easy-to-implement. Nevertheless, in the

scientific literature[19-23] several papers prove that the use of this method is effective for solving trajectory optimization problems.

In this work the optimal control problem involves continuous time-dependent control variables and can be translated into a parameter optimization problem through the first-order necessary conditions for optimality, which allow expressing the control variables as functions of the adjoint variables conjugate to the dynamics equations. The parameter set includes $\{\lambda_{10}, \lambda_{40}, \lambda_{50}, t_f\}$. The boundary conditions are represented by the three equality constraints [12] for r_f , v_{rf} , and v_{tf} , accompanied by the inequality constraint [26]. Once the optimal parameter set has been determined, the (planar) state and costate equations can be integrated, using Eq. [22] to express the control angle α as a function of the adjoint variables.

For the problem at hand the PSO algorithm employs 100 particles and is run for 500 iterations. The problem is solved by employing a set of canonical units: the Moon radius represents the distance unit $(1\ \text{DU} = 1738\ \text{km})$, whereas the time unit is such that $\mu = 1\ \text{DU}^3/\text{TU}^2$ (i.e. $1\ \text{TU} = 1034.8\ \text{sec}$). The search space is defined by the inequalities $-1 \le \lambda_{k0} \le 1 \quad (k = 1,3,4)$ and $0.5\ \text{TU} \le t_f \le 3\ \text{TU}$. It is worth remarking that the ignorability of the parameter condition allows defining arbitrarily the range in which the initial values of the adjoint variables are sought. The swarming algorithm is capable of obtaining the optimal (planar) ascent trajectory with great accuracy. In fact, the errors on the desired final conditions are $\left|r_f^* - (R_M + h_P)\right| = 1.158 \cdot 10^{-12}$ km , $\left|v_{rf}^*\right| = 3.152 \cdot 10^{-15}$ km/sec , and $\left|v_{tf}^* - \sqrt{\frac{\mu}{a}\frac{1+e}{1-e}}\right| = 3.356 \cdot 10^{-15}$ km/sec , whereas the minimum time turns out to be $t_f^* = 9.576$ min . Figures II through V portray the state components associated with the optimal ascent trajectory and the related optimal control time history.

The PSO algorithm uses the first-order necessary conditions to determine the optimal trajectory. However, the second-order conditions are also to be satisfied for applying the neighboring optimal guidance using the optimal ascent path as the reference, nominal trajectory. Evaluation of the matrices H_{uu} and Ŝ along the optimal path allows verifying that the second-order sufficient conditions for a minimum are both satisfied, and this represents the theoretical premise for a successful application of VTD-NOG.

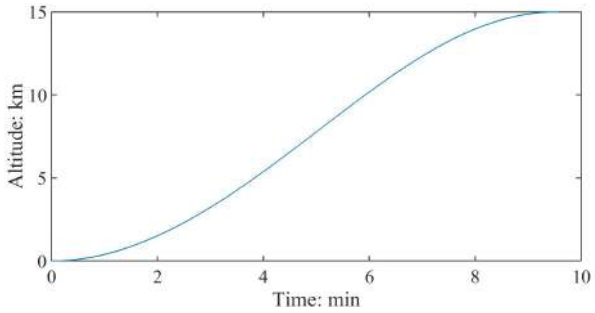

Fig. II: Optimal ascent path: altitude time history

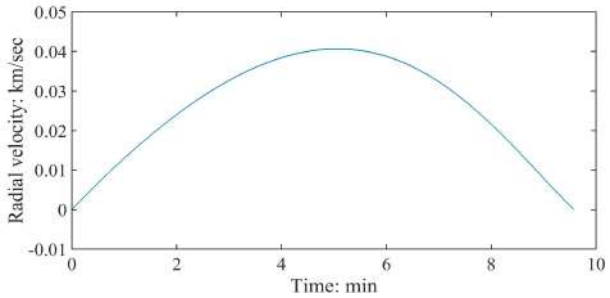

Fig. III: Optimal ascent path: radial velocity time history

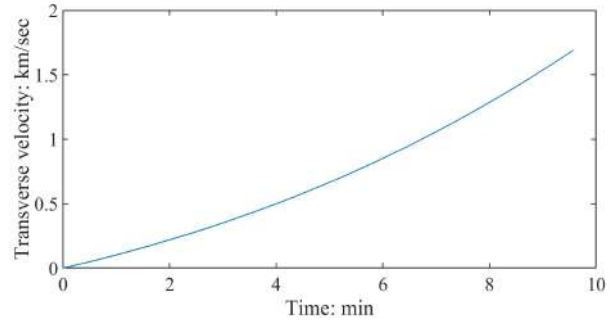

Fig. IV: Optimal ascent path: transverse velocity time history

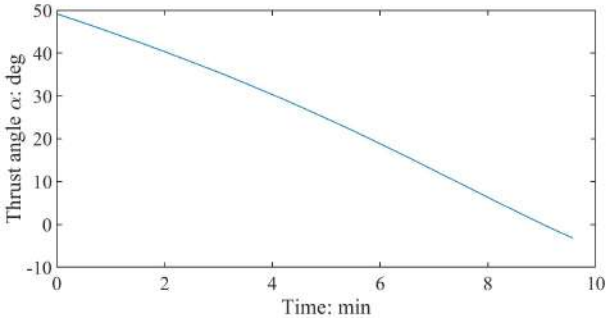

Fig. V: Optimal ascent path: thrust angle time history

III. VARIABLE-TIME-DOMAIN NEIGHBORING OPTIMAL GUIDANCE

The Variable-Time-Domain Neighboring Optimal Guidance (VTD-NOG) uses the optimal trajectory as the reference path, with the final intent of determining the control correction at each sampling time $\{t_k\}_{k=0,\ldots,n_S}$, with $t_0 = 0$. These are the times at which the displacement between the actual trajectory, associated with $\boldsymbol{x}$, and the nominal trajectory, corresponding to $\boldsymbol{x}^*$, is evaluated, to yield

$$d\boldsymbol{x}_k \equiv \delta\boldsymbol{x}_k = \boldsymbol{x}(t_k) - \boldsymbol{x}^*(t_k), \quad \text{with} \quad t_k = \tau_k t_f^{(k)} \quad [57]$$

where $t_f^{(k)}$ denotes the overall time of flight calculated at time t_k. The total number of sampling times, n_S, is unspecified, whereas the actual time interval between two successive sampling times is given and denoted with Δt_S, $\Delta t_S = t_{k+1} - t_k \quad (k = 0,\ldots,n_S - 1)$. It is apparent that a fundamental ingredient needed to implement VTD-NOG is the formula for determining $t_f^{(k)}$ at t_k.

III.I Time-to-go updating law and termination criterion

The fundamental principle that underlies the VTD-NOG scheme consists in finding the control correction $\delta\boldsymbol{u}(\tau)$ in the generic interval $[\tau_k, \tau_{k+1}]$ such that the second differential of J is minimized[13], while holding the first-order expansions of the state equations, the related final conditions, and the parameter condition (i.e. the second of Eq. [33]). In contrast, the first of Eq. [33] cannot be used, because in general $\delta\boldsymbol{\mu}_k \neq \mathbf{0}$ at τ_k. Minimizing the second differential of J is equivalent to solving the accessory optimization problem, defined in the interval $[\tau_k, 1]$. The solution of the same problem in the overall interval $[0,1]$ leads to deriving all the relations reported in the previous section and in Ref. 13. This means that the latter relations need to be extended to the generic interval $[\tau_k, 1]$. Other than the linear expansion of the state and costate equations and the related boundary conditions, and the second of Eq. [33], also Eq. [31] remains unchanged. Equation [34] yields the control correction in the interval $\tau_k \le \tau \le \tau_{k+1}$.

Following the same steps described in Ref. 13, Eqs. [35] through [37] and can be derived again, but are not reported for the sake of conciseness. However, Eq. [55], which derives from Eqs. [45]-[46], is now to be evaluated at τ_k and becomes

$$\begin{bmatrix} d\boldsymbol{v} \\ d\boldsymbol{a} \end{bmatrix} = -\mathbf{V}_k^{-1}\mathbf{U}_k^T\delta\boldsymbol{x}_k - \mathbf{V}_k^{-1}\boldsymbol{\Theta}\delta\boldsymbol{\mu}_k \quad \text{with} \quad \boldsymbol{\Theta} := \begin{bmatrix} \mathbf{0}_{qxp} \\ \mathbf{I}_{pxp} \end{bmatrix} \quad [58]$$

because $\delta\boldsymbol{\mu}_k \neq \mathbf{0}$ (unlike $\delta\boldsymbol{\mu}_0 = \mathbf{0}$). The symbols $\mathbf{0}_{qxp}$ and $\mathbf{I}_{pxp}$ denote respectively the null and the identity matrices, with dimensions indicated in the subscript. The latter relation supplies the corrections $d\boldsymbol{v}$ and $d\boldsymbol{a}$ at τ_k as functions of the gain matrices **U** and **V** (defined in Eq. [56]), $\delta\boldsymbol{x}_k$ (evaluated at τ_k, cf. Eq. [57]), and $\delta\boldsymbol{\mu}_k$ (coming from the numerical integration of Eq. [37] in the preceding interval $[\tau_{k-1}, \tau_k]$). Actually, Eq. [58] contains the updating law of the total flight time t_f, which is included as a component of $\boldsymbol{a}$. Hence, if $dt_f^{(k)}$ denotes the correction on t_f^* evaluated at τ_k, then

$$t_f^{(k)} = t_f^* + dt_f^{(k)} \quad [59]$$

If the actual sampling interval Δt_S is specified, the general formula for τ_k is

$$\tau_{k+1} = \sum_{j=0}^{k} \frac{\Delta t_S}{t_f^{(j)}} \qquad (k = 1,\ldots,n_S - 1) \quad [60]$$

The overall number of intervals n_S is found at the first occurrence of the following condition:

$$\sum_{j=0}^{n_S} \frac{\Delta t_S}{t_f^{(j)}} \ge 1 \quad \Rightarrow \quad \tau_{n_S+1} = 1 \quad [61]$$

It is worth stressing that the updating formula [59] derives directly from the natural extension of the accessory optimization problem to the time interval $[\tau_k, 1]$. In addition, the introduction of the normalized time τ now reveals its great utility. In fact, all the gain matrices are defined in the normalized interval [0,1] and cannot become singular. Moreover, the limiting values $\{\tau_k\}_{k=1,\ldots,n_S-1}$ are dynamically calculated at each sampling time using Eq. [60], while the sampling instants in the actual time domain are specified and equally-spaced. Also the termination criterion has a logical, consistent definition, and corresponds to the upper bound of the interval [0,1[, to which τ is constrained.

III.II Modified sweep method

The definition of a neighboring optimal path requires the numerical backward integration of the sweep equations. A suitable integration technique is based on using the classical sweep equations in the interval $[\tau_{sw}, 1]$ (where τ_{sw} is sufficiently close to $\tau_f = 1$) and then switching to $\hat{\mathbf{s}}$. However, due to Eq. [58], new relations are to be derived for $\hat{\mathbf{s}}$ and the related matrices.

First, after inserting Eq. [58] (evaluated at the generic τ) into Eq. [44] one obtains

$$\delta\boldsymbol{\lambda} = \hat{\mathbf{S}}\delta\boldsymbol{x} - \mathbf{W}\delta\boldsymbol{\mu} \qquad \text{with} \qquad \mathbf{W} \coloneqq \mathbf{U}\mathbf{V}^{-1}\boldsymbol{\Theta} \quad [62]$$

Due to Eq. [46], the latter relation can be rewritten as

$$\delta\boldsymbol{\lambda} = \left(\hat{\mathbf{S}} - \mathbf{W}\mathbf{m}^T\right)\delta\boldsymbol{x} - \mathbf{W}\mathbf{n}^T d\nu - \mathbf{W}\boldsymbol{\alpha} da \quad [63]$$

This relation replaces Eq. [44].

Considerable analytical developments[24,25] (not reported for the sake of conciseness) lead to the following modified sweep equations:

$$\dot{\hat{\mathbf{S}}} = -\hat{\mathbf{S}}\mathbf{A} + \hat{\mathbf{S}}\mathbf{B}\hat{\mathbf{S}} + \left[\hat{\mathbf{S}}\mathbf{D}\boldsymbol{\alpha}^{-1} + \mathbf{W}\mathbf{F}\boldsymbol{\alpha}^{-1} + \mathbf{E}\boldsymbol{\alpha}^{-1}\right]\mathbf{m}^T - \mathbf{W}\mathbf{E}^T - \mathbf{W}\mathbf{D}^T\hat{\mathbf{S}} - \mathbf{C} - \mathbf{A}^T\hat{\mathbf{S}} \quad [64]$$

$$\dot{\mathbf{R}}^T = \mathbf{R}^T\mathbf{B}\hat{\mathbf{S}} - \mathbf{R}^T\mathbf{A} - \mathbf{R}^T\mathbf{B}\mathbf{W}\mathbf{m}^T \quad [65]$$

$$\dot{\mathbf{Q}} = -\mathbf{R}^T\mathbf{B}\mathbf{W}\mathbf{n}^T \quad [66]$$

$$\dot{\mathbf{n}} = -\mathbf{R}^T\left(\mathbf{D} + \mathbf{B}\mathbf{W}\boldsymbol{\alpha}\right) \quad [67]$$

$$\dot{\mathbf{m}}^T = -\mathbf{m}^T\mathbf{A} + \mathbf{m}^T\mathbf{B}\hat{\mathbf{S}} - \mathbf{m}^T\mathbf{B}\mathbf{W}\mathbf{m}^T - \mathbf{E}^T - \mathbf{D}^T\hat{\mathbf{S}} + \mathbf{D}^T\mathbf{W}\mathbf{m}^T \quad [68]$$

$$\dot{\boldsymbol{\alpha}} = \mathbf{D}^T\mathbf{W}\boldsymbol{\alpha} - \mathbf{F} - \mathbf{m}^T\mathbf{B}\mathbf{W}\boldsymbol{\alpha} - \mathbf{m}^T\mathbf{D} \quad [69]$$

In the end, the gain matrices involved in the sweep method, i.e. **S**, $\hat{\mathbf{S}}$, **R**, **Q**, **n**, **m**, and $\boldsymbol{\alpha}$, can be backward integrated in two steps:

(a) in the interval $[\tau_{sw}, 1]$ the equations of the classical sweep method[13], with the respective boundary conditions are used,

(b) in the interval $[0, \tau_{sw}]$ Eqs. [64], [65]-[67], [68], and [69] are used. The matrices **R**, **Q**, **n**, **m**, and $\boldsymbol{\alpha}$ are continuous across the switching time τ_{sw}, whereas $\hat{\mathbf{S}}$ is given by $\hat{\mathbf{S}} \coloneqq \mathbf{S} - \mathbf{U}\mathbf{V}^{-1}\mathbf{U}^T$; in this work τ_{sw} is set to 0.99.

III.III Preliminary offline computations

The implementation of NOG requires several preliminary computations that can be completed offline and stored in the onboard computer.

First of all, the optimal trajectory is to be determined, together with the related state, costate, and control variables, which are assumed as the nominal ones. In the time domain τ these can be either available analytically or represented as sequences of equally-spaced values, e.g.

$$\boldsymbol{u}_i^* = \boldsymbol{u}^*(\tau_i) \qquad (i = 0, \ldots, n_D;\ \tau_0 = 0 \text{ and } \tau_{n_D} = 1) \quad [70]$$

However, in the presence of perturbations, NOG determines the control corrections $\delta\boldsymbol{u}(\tau)$ in each interval $[\tau_k, \tau_{k+1}]$, where the values $\{\tau_k\}$ never coincide with the equally-spaced values $\{\tau_i\}$ of Eq. [70]. Hence, regardless of the number of points used to represent the control correction $\delta\boldsymbol{u}(\tau)$ in $[\tau_k, \tau_{k+1}]$, it is apparent that a suitable interpolation is to be adopted for the control variable $\boldsymbol{u}^*$ (provided that no analytical expression is available). In this way, the value of $\boldsymbol{u}^*$ can be evaluated at any arbitrary time in the interval $0 \le \tau \le 1$. For the same reason also the nominal state $\boldsymbol{x}^*$ and costate $\boldsymbol{\lambda}^*$ need to be interpolated. If a sufficiently large number of points is selected (e.g., $n_D = 1001$), then piecewise linear interpolation is a suitable option. The successive step is the analytical derivation of the matrices

$$\{\boldsymbol{f}_x, \boldsymbol{f}_u, \boldsymbol{f}_a, H_{xx}, H_{xu}, H_{x\lambda}, H_{xa}, H_{ux}, H_{uu}, H_{ua}, H_{u\lambda}, H_{ax}, H_{au}, H_{aa}, H_{a\lambda}, \boldsymbol{\psi}_{x_f}, \boldsymbol{\psi}_{x_0}, \boldsymbol{\psi}_a, \tilde{\Phi}_{x_0x_0}, \tilde{\Phi}_{x_0a}, \tilde{\Phi}_{x_fx_f}, \tilde{\Phi}_{x_fa}, \tilde{\Phi}_{ax_f}, \tilde{\Phi}_{aa}\} \quad [71]$$

Then, they are evaluated along the nominal trajectory, and used to define also the matrices **A**, **B**, **C**, **D**, **E**, and **F**. Each element of these matrices, together with those of the matrices of Eq. [71], are linearly interpolated. Subsequently, the two-step backward integration of the sweep equations described in Section III.II is performed and yields the gain matrices $\hat{\mathbf{S}}$, **R**, **m**, **Q**, **n**, and $\boldsymbol{\alpha}$, using also the analytic expressions of **W**, **U**, and **V** (written in terms of **R**, **m**, **Q**, **n**, and $\boldsymbol{\alpha}$). The linear interpolation of all the matrices not yet interpolated concludes the preliminary computations.

III.IV VTD-NOG algorithm structure

On the basis of the optimal reference path, using the nominal quantities (vectors and matrices) computed offline, at each time τ_k the VTD-NOG algorithm determines the time of flight and the control correction. More specifically, the following steps implement the feedback guidance scheme:

1. Set the actual sampling time interval Δt_S.
2. At each time τ_k $(k = 0, \ldots, n_S - 1;\ \tau_0 = 0)$
   a. Evaluate $\delta\boldsymbol{x}_k$ through Eq. [57];
   b. Assume the value of $\delta\boldsymbol{\mu}$ calculated at the end of the previous interval $[\tau_{k-1}, \tau_k]$ as $\delta\boldsymbol{\mu}_k$ $(\delta\boldsymbol{\mu}_0 = \mathbf{0})$;
   c. Calculate the correction $dt_f^{(k)}$ and the updated time of flight $t_f^{(k)}$ by means of Eqs. [58]-[59];
   d. Calculate the limiting value τ_{k+1} using Eq. [60];
   e. Evaluate $\delta\boldsymbol{\lambda}_k$ through Eq. [63];
   f. Integrate numerically the linear differential system composed of Eqs. [35]-[37], in the interval $[\tau_k, \tau_{k+1}]$;
   g. Determine the control correction $\delta\boldsymbol{u}(\tau)$ in $[\tau_k, \tau_{k+1}]$ through Eq. [34].

3. If Eq. [61] holds, then VTD-NOG terminates, otherwise point 2 is repeated after increasing k by 1.

Figure VI portrays a block diagram that illustrates the sample-data feedback structure of the NOG algorithm, in which the control and flight time corrections definitely depend on the state displacement $\delta \boldsymbol{x}$ (evaluated at specified discrete times) through the time-varying gain matrices, which are computed offline and stored onboard. The attitude control loop (encircled by the dotted line) is being described in detail in the following.

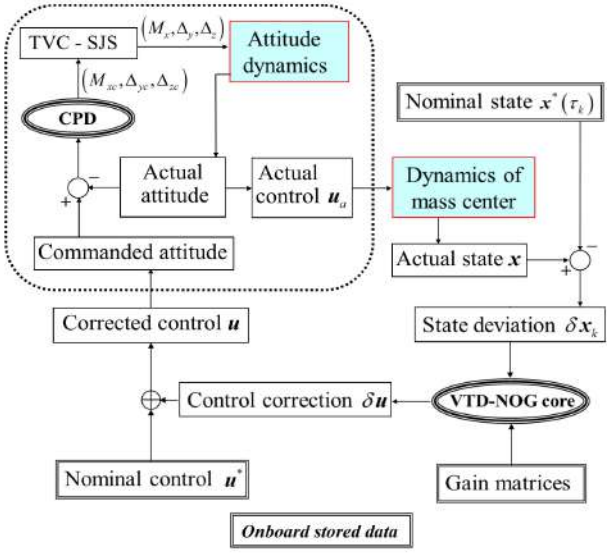

Fig. VI: Block diagram of VTD-NOG & CPD

IV. CONSTRAINED PROPORTIONAL-DERIVATIVE ATTITUDE CONTROL

The attitude control system is designed for the purpose of guaranteeing the correct spacecraft orientation, on the basis of the corrected control $\boldsymbol{u}$ yielded iteratively by VTD-NOG. The output of the attitude control system is represented by the actual control $\boldsymbol{u}_a$ (cf. Fig. VI).

IV.I Commanded attitude

With reference to Fig. VI, VTD-NOG yields the corrected control $\boldsymbol{u}$, i.e. the thrust direction identified by the angles α and β, under the approximating assumption that this direction is always aligned with the longitudinal axis of the spacecraft. This means that these two corrected angles represent the commanded values, denoted with α_c and β_c, that the attitude control system must pursue through the use of thrust vectoring.

Let $(\hat{a}_1,\hat{a}_2,\hat{a}_3)$ denote an auxiliary inertial frame defined as

$$\hat{a}_1=\hat{c}_2 \quad \hat{a}_2=-\hat{c}_3 \quad \hat{a}_3=-\hat{c}_1 \qquad [72]$$

The rotation matrix $\mathbf{R}_A$ relates the two inertial frames, i.e. $\begin{bmatrix}\hat{a}_1 & \hat{a}_2 & \hat{a}_3\end{bmatrix}^T=\mathbf{R}_A\begin{bmatrix}\hat{c}_1 & \hat{c}_2 & \hat{c}_3\end{bmatrix}^T$. The spacecraft instantaneous orientation is associated with the body frame $(\hat{x}_b,\hat{y}_b,\hat{z}_b)$, whose origin is in the instantaneous center of mass of the vehicle, its axes coincide with the principal axes of inertia, and $\hat{x}_b$ is aligned with the longitudinal axis. The body frame is obtained from the inertial frame $(\hat{a}_1,\hat{a}_2,\hat{a}_3)$ through a sequence of three elementary counterclockwise rotations, about axes 3, 2, and 1,

$$\begin{bmatrix}\hat{x}_b & \hat{y}_b & \hat{z}_b\end{bmatrix}^T=\mathbf{R}_1(\Phi)\mathbf{R}_2(\Theta)\mathbf{R}_3(\Psi)\begin{bmatrix}\hat{a}_1 & \hat{a}_2 & \hat{a}_3\end{bmatrix}^T \qquad [73]$$

The angles Ψ, Θ, and Φ are the yaw, pitch, and roll angle, respectively. The respective commanded values are denoted with Ψ_c, Θ_c, and Φ_c, and correspond to a thrust direction $\hat{T}_c$ that points toward $\hat{x}_b$. This alignment condition leads to

$$\hat{T}_c=\begin{bmatrix}\cos\Theta_c\cos\Psi_c & \cos\Theta_c\sin\Psi_c & -\sin\Theta_c\end{bmatrix}\cdot \begin{bmatrix}\hat{a}_1 & \hat{a}_2 & \hat{a}_3\end{bmatrix}^T \qquad [74]$$

On the other hand, the commanded thrust direction is identified through the two angles α_c and β_c:

$$\begin{aligned}\hat{T}_c&=\begin{bmatrix}\cos\beta_c\sin\alpha_c & \cos\beta_c\cos\alpha_c & \sin\beta_c\end{bmatrix}\begin{bmatrix}\hat{r} & \hat{t} & \hat{n}\end{bmatrix}^T\\&=\begin{bmatrix}\cos\beta_c\sin\alpha_c & \cos\beta_c\cos\alpha_c & \sin\beta_c\end{bmatrix}\cdot\\&\quad\mathbf{R}_2(-\phi)\mathbf{R}_3(\xi)\mathbf{R}_A^T\begin{bmatrix}\hat{a}_1 & \hat{a}_2 & \hat{a}_3\end{bmatrix}^T\\&=:\begin{bmatrix}T_{c1} & T_{c2} & T_{c3}\end{bmatrix}\begin{bmatrix}\hat{a}_1 & \hat{a}_2 & \hat{a}_3\end{bmatrix}^T\end{aligned} \qquad [75]$$

where the components T_{ci} $(i=1,2,3)$ are introduced, and are expressed in terms of α_c, β_c, ϕ, and ξ. Identification of Eqs. [74] and [75] leads to obtaining Ψ_c and Θ_c as functions of α_c, β_c, ϕ, and ξ:

$$\Theta_c=-\arcsin T_{c3} \qquad [76]$$

$$\sin\Psi_c=\frac{T_{c2}}{\cos\Theta_c} \quad \text{and} \quad \cos\Psi_c=\frac{T_{c1}}{\cos\Theta_c} \qquad [77]$$

The commanded roll angle Φ_c is independent of $\hat{T}_c$, and can be selected on the basis of practical requirements, for instance in order to attain a convenient alignment for sensors, solar panels, or antennas.

IV.II Attitude dynamics

Thrust vector control (TVC) is used to control pitch and yaw motion of the lunar module, and side jet system (SJS) is used to control roll motion. The attitude of the

body frame with respect to the auxiliary inertial frame $(\hat{a}_1, \hat{a}_2, \hat{a}_3)$ is here represented by quaternions (q_1, q_2, q_3, q_4) instead of the angles Ψ, Θ, and Φ, since the spacecraft is subject to relatively large attitude maneuvers. The attitude kinematics equations are given by[26]

$$\begin{bmatrix} \dot{q}_1 \\ \dot{q}_2 \\ \dot{q}_3 \\ \dot{q}_4 \end{bmatrix} = \frac{1}{2} \begin{bmatrix} 0 & R & -Q & P \\ -R & 0 & P & Q \\ Q & -P & 0 & R \\ -P & -Q & -R & 0 \end{bmatrix} \begin{bmatrix} q_1 \\ q_2 \\ q_3 \\ q_4 \end{bmatrix} \quad [78]$$

where P, Q, R are the body coordinates of the angular velocity of the lunar module. The attitude dynamics equations are given by

$$\dot{P} = \frac{I_y - I_z}{I_x} QR + \frac{1}{I_x}\left(M_x + M_{gx}\right) \quad [79]$$

$$\dot{Q} = \frac{I_z - I_x}{I_y} PR + \frac{1}{I_y}\left(Tl \cos\Delta_z \sin\Delta_y + M_{gy}\right) \quad [80]$$

$$\dot{R} = \frac{I_x - I_y}{I_z} PQ + \frac{1}{I_z}\left(-Tl \sin\Delta_z + M_{gz}\right) \quad [81]$$

where I_x, I_y, and I_z are the principal moments of inertia, M_x is the torque generated by the side jet system, T is the thrust amplitude, and l is the distance between the center of mass and the swivel point of the TVC, which lies on the longitudinal axis. Variables Δ_y and Δ_z denote the thrust deflection angles portrayed in Fig. VII. The symbols M_{gx}, M_{gy}, and M_{gz} represent the coordinates of the gravity gradient torque along the body axes.[27]

The electro-hydraulic servoactuator that controls the engine deflection angles is here modeled by the following two first-order systems:[16]

$$\dot{\tilde{\Delta}}_y = -\frac{1}{\tau_y}\tilde{\Delta}_y + \frac{1}{\tau_y}\Delta_{yc} \quad [82]$$

$$\dot{\tilde{\Delta}}_z = -\frac{1}{\tau_z}\tilde{\Delta}_z + \frac{1}{\tau_z}\Delta_{zc} \quad [83]$$

In Eq. [82] Δ_{yc} is the commanded Δ_y and represents one of the three control inputs for the attitude control system, while the actual angle Δ_y (appearing in Eq. [80]) is obtained by saturating $\tilde{\Delta}_y$ to its maximum value $\bar{\Delta}_y$,

$$\Delta_y = \text{sat}_{\bar{\Delta}_y}\left(\tilde{\Delta}_y\right) = \begin{cases} -\bar{\Delta}_y & \text{if} \quad \tilde{\Delta}_y < -\bar{\Delta}_y \\ \Delta_y & \text{if} \quad -\bar{\Delta}_y \le \tilde{\Delta}_y \le \bar{\Delta}_y \\ \bar{\Delta}_y & \text{if} \quad \tilde{\Delta}_y > \bar{\Delta}_y \end{cases} \quad [84]$$

Similar considerations apply to Eq. [83], thus Δ_{zc} represents a control input, and $\bar{\Delta}_z$ is the saturation value for $\tilde{\Delta}_z$. The actuator of the side jet system is model by the following first order system:

$$\dot{\tilde{M}}_x = -\frac{1}{\tau_x}\tilde{M}_x + \frac{1}{\tau_x}M_{xc} \quad [85]$$

for which similar considerations apply. In particular, M_{xc} is the commanded M_x, and represents the third control input for the attitude control system. Moreover, the saturation value for $\tilde{M}_x$ is denoted with $\bar{M}_x$.

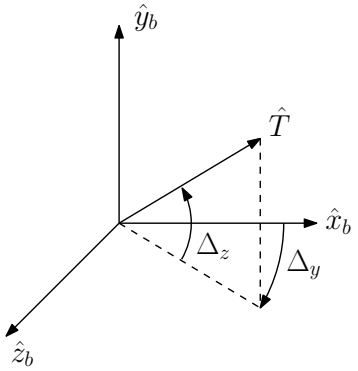

Fig. VII: Thrust deflection angles

The commanded quaternions, denoted with $(q_{c1}, q_{c2}, q_{c3}, q_{c4})$, are derived directly from the commanded angles Φ_c, Θ_c, and Ψ_c provided by the VTD-NOG algorithm, as discussed in subsection IV.I. Commanded quaternions are then used to generate the attitude-error quaternions $(q_{e1}, q_{e2}, q_{e3}, q_{e4})$, as follows[26]

$$\begin{bmatrix} q_{e1} \\ q_{e2} \\ q_{e3} \\ q_{e4} \end{bmatrix} = \begin{bmatrix} q_{c4} & q_{c3} & -q_{c2} & -q_{c1} \\ -q_{c3} & q_{c4} & q_{c1} & -q_{c2} \\ q_{c2} & -q_{c1} & q_{c4} & -q_{c3} \\ q_{c1} & q_{c2} & q_{c3} & q_{c4} \end{bmatrix} \begin{bmatrix} q_1 \\ q_2 \\ q_3 \\ q_4 \end{bmatrix} \quad [86]$$

IV.III Control algorithm

A baseline attitude control action for such spacecraft is given by the following PD control:

$$M_{xc} = -k_{px}q_{e1} - k_{dx}P \quad [87]$$

$$\Delta_{yc} = -k_{py}q_{e2} - k_{dy}Q \quad [88]$$

$$\Delta_{zc} = k_{pz}q_{e3} + k_{dz}R \quad [89]$$

To analyze convergence properties achieved by the considered controller, first it is worth noticing that most of times the quaternions $(q_{c1}, q_{c2}, q_{c3}, q_{c4})$ can be modeled as constant since the guidance command usually changes slowly compared to attitude maneuvers. Next, it will be shown that if $(q_{c1}, q_{c2}, q_{c3}, q_{c4})$ is constant, then the proposed PD control guarantees local

convergence to the desired attitude. In fact, if $(q_{c1}, q_{c2}, q_{c3}, q_{c4})$ is constant, then the attitude-error quaternions satisfy the differential equation obtained by replacing in Eq. [78] q_1 with q_{e1}, q_2 with q_{e2}, and so on[28]. Thus, linearizing the latter differential equation and Eqs. [79] through [81] about the identity attitude-error quaternions $(q_{e1}, q_{e2}, q_{e3}, q_{e4}) = (0,0,0,1)$, zero angular velocity $P = Q = R = 0$, and zero output for all actuators $M_x = \Delta_y = \Delta_z = 0$, the following relations are obtained:

$$\dot{q}_{e1} = \frac{1}{2}P \qquad \dot{q}_{e2} = \frac{1}{2}Q \qquad \dot{q}_{e3} = \frac{1}{2}R \qquad [90]$$

$$\dot{P} = \frac{1}{I_x}M_x \qquad \dot{Q} = \frac{Tl}{I_y}\Delta_y \qquad \dot{R} = -\frac{Tl}{I_z}\Delta_z \qquad [91]$$

Moreover, linearization of the actuator's equations in Eqs. [82] and [84] about $\tilde{\Delta}_y = 0$ leads to

$$\dot{\Delta}_y = -\frac{1}{\tau_y}\Delta_y + \frac{1}{\tau_y}\Delta_{yc} \qquad [92]$$

By applying analogous linearization process to the other actuators' equations one obtains

$$\dot{\Delta}_z = -\frac{1}{\tau_z}\Delta_z + \frac{1}{\tau_z}\Delta_{zc} \qquad \dot{M}_x = -\frac{1}{\tau_x}M_x + \frac{1}{\tau_x}M_{xc} \quad [93]$$

Note that equations relative to each single axis are decoupled from the others. Then, it is easy to obtain that the linearized closed-loop system given by Eqs. [87]-[93] is asymptotically stable if $k_{dx} > k_{px}\tau_x > 0$, $k_{dy} > k_{py}\tau_y > 0$, and $k_{dz} > k_{pz}\tau_z > 0$.

The considered PD control can lead to excessive rates for the thrust deflection angles Δ_y and Δ_z and roll control torque M_x. In fact, high values for the gains k_{px}, k_{dx}, k_{py}, k_{dy}, k_{pz}, and k_{dz} might be required to obtain a fast response of the attitude control system in comparison with the guidance command. Then, high gains can in turn lead to high amplitudes for the rates of M_x, Δ_y, and Δ_z. If the rates are too high, then clearly they become physically infeasible. The latter issue is here tackled by using Constrained Proportional and Derivative (CPD) control, which is described by the following equations:

$$\begin{aligned} M_{xc} &= -\mathrm{sat}_{\bar{M}_{xc}}\left(k_{px}q_{e1} + k_{dx}P\right) \\ \Delta_{yc} &= -\mathrm{sat}_{\bar{\Delta}_{yc}}\left(k_{py}q_{e2} + k_{dy}Q\right) \\ \Delta_{zc} &= \mathrm{sat}_{\bar{\Delta}_{zc}}\left(k_{pz}q_{e3} + k_{dz}R\right) \end{aligned} \qquad [94]$$

which replace Eqs. [87], [88], and [89], respectively. In Eq. [94] $\bar{M}_{xc} > 0$, $\bar{\Delta}_{yc} > 0$, and $\bar{\Delta}_{zc} > 0$ are additional design parameters.

It will be shown next that employing CPD control in Eq. [94] ensures that

$$\left|\dot{M}_x\right| \le \frac{2}{\tau_x}\bar{M}_{xc} \qquad \left|\dot{\Delta}_y\right| \le \frac{2}{\tau_y}\bar{\Delta}_{yc} \qquad \left|\dot{\Delta}_z\right| \le \frac{2}{\tau_z}\bar{\Delta}_{zc} \quad [95]$$

assuming that $M_x(0) = 0$ and $\Delta_y(0) = \Delta_y(0) = 0$. Thus, an appropriate choice of $\bar{M}_{xc}$, $\bar{\Delta}_{yc}$, and $\bar{\Delta}_{zc}$ guarantees that $\dot{M}_x$, $\dot{\Delta}_y$, and $\dot{\Delta}_z$ do not exceed physical limits. To show that the second inequality in Eq. [95] holds, first note that Eqs. [82] and [94] imply

$$\left|\ddot{\tilde{\Delta}}_y\right| \le \frac{1}{\tau_y}\left|\tilde{\Delta}_y\right| + \frac{1}{\tau_y}\bar{\Delta}_{yc} \qquad [96]$$

$$\ddot{\tilde{\Delta}}_y \le -\frac{1}{\tau_y}\tilde{\Delta}_y + \frac{1}{\tau_y}\bar{\Delta}_{yc} \quad \text{and} \quad -\ddot{\tilde{\Delta}}_y \le \frac{1}{\tau_y}\tilde{\Delta}_y + \frac{1}{\tau_y}\bar{\Delta}_{yc} \quad [97]$$

Thus, considering that $\tilde{\Delta}_y(0) = 0$ and using the Comparison Lemma[29], it is easy to obtain that

$$\left|\tilde{\Delta}_y\right| \le \bar{\Delta}_{yc} \qquad [98]$$

Then, the second inequality of Eq. [95] follows directly from Eqs. [84], [96], and [98]. Parallel arguments can be used to show the validity of the other two inequalities in Eq. [95].

It is worth noticing that linearization of CPD control in Eq. [94] about $q_{e1} = q_{e2} = q_{e3} = 0$ and $P = Q = R = 0$, clearly reduces CPD to the standard PD control in Eqs. [87]-[89]. Thus, also CPD control achieves local convergence to the desired attitude.

IV.IV Determination of control gains

The goal of the current subsection is presenting a method for determining at least first guess values for the gains k_{px}, k_{py}, k_{pz}, k_{dx}, k_{dy}, and k_{dz}. The method is here illustrated only for gains k_{py} and k_{dy}, because it can be easily extended to the other gains. Neglect dynamics of the actuator in Eq. [82] and consider the linearized closed-loop system in Eqs. [88] and [90]-[91], obtaining

$$\ddot{q}_{e2} = \frac{Tl}{2I_y}\left(-k_{py}q_{e2} - 2k_{dy}\dot{q}_{e2}\right) \qquad [99]$$

Thus, the corresponding characteristic equation in the Laplace domain is given by

$$s^2 + 2G_y k_{dy} s + G_y k_{py} = 0 \qquad [100]$$

where $G_y = Tl/(2I_y)$. Note that the value of G_y varies during the flight since so do the values of T, l, and I_y. Let $\underline{G_y}$ and $\overline{G_y}$ be the minimum and maximum values of G_y along the considered flight. Then, the gains k_{py} and k_{dy} are chosen so that for all $\underline{G_y} \le G_y \le \overline{G_y}$ it

occurs that the solutions of Eq. [100] have damping ratio $\zeta_y \geq \underline{\zeta_y}$ and natural angular frequency $\omega_{ny} \geq \underline{\omega_{ny}}$. Magnitudes $\underline{\zeta_y}$ and $\underline{\omega_{ny}}$ are chosen based on experience and proceeding by trial-and-error. Since $G_y k_{py} = \omega_{ny}^2$ and $G_y k_{dy} = \zeta_y \omega_{ny}$, then it is easy to verify that the specifications $\zeta_y \geq \underline{\zeta_y}$ and $\omega_{ny} \geq \underline{\omega_{ny}}$ are fulfilled for all $\underline{G_y} \leq G_y \leq \overline{G_y}$ by setting

$$k_{py} = \underline{\omega_{ny}^2} / \underline{G_y} \qquad k_{dy} = \underline{\zeta_y}\, \underline{\omega_{ny}} / \underline{G_y} \tag{101}$$

IV.V Actual attitude and thrust angles

The actual spacecraft orientation is defined by the instantaneous values of the quaternions (q_1, q_2, q_3, q_4), associated with the rotation matrix $\mathbf{R}_Q$[27]:

$$\begin{aligned} \begin{bmatrix} \hat{x}_b & \hat{y}_b & \hat{z}_b \end{bmatrix}^T &= \mathbf{R}_Q \begin{bmatrix} \hat{a}_1 & \hat{a}_2 & \hat{a}_3 \end{bmatrix}^T \\ &= \mathbf{R}_Q \mathbf{R}_A \mathbf{R}_3(-\xi) \mathbf{R}_2(\phi) \begin{bmatrix} \hat{r} & \hat{t} & \hat{n} \end{bmatrix}^T \end{aligned} \tag{102}$$

Moreover, the actual thrust direction $\hat{T}_a$ depends on the two angles Δ_y and Δ_z:

$$\begin{aligned} \hat{T}_a = &\begin{bmatrix} \cos\Delta_y \cos\Delta_z & \sin\Delta_z & \cos\Delta_z \sin\Delta_y \end{bmatrix} \cdot \\ &\begin{bmatrix} \hat{x}_b & \hat{y}_b & \hat{z}_b \end{bmatrix}^T \end{aligned} \tag{103}$$

Due to Eq. [102], the last relation can be rewritten as

$$\begin{aligned} \hat{T}_a = &\begin{bmatrix} \cos\Delta_y \cos\Delta_z & \sin\Delta_z & \cos\Delta_z \sin\Delta_y \end{bmatrix} \cdot \\ &\mathbf{R}_Q \mathbf{R}_A \mathbf{R}_3(-\xi) \mathbf{R}_2(\phi) \begin{bmatrix} \hat{r} & \hat{t} & \hat{n} \end{bmatrix}^T \\ =: &\begin{bmatrix} T_{a1} & T_{a2} & T_{a3} \end{bmatrix} \begin{bmatrix} \hat{r} & \hat{t} & \hat{n} \end{bmatrix}^T \end{aligned} \tag{104}$$

where the components T_{ai} $(i = 1,2,3)$ are introduced, and are expressed in terms of (q_1, q_2, q_3, q_4), ϕ, ξ, Δ_y, and Δ_z.

However, in the $(\hat{r}, \hat{t}, \hat{n})$-frame the actual thrust direction can be written also as a function of the two actual thrust angles α_a and β_a:

$$\begin{aligned} \hat{T}_a = &\begin{bmatrix} \cos\beta_a \sin\alpha_a & \cos\beta_a \cos\alpha_a & \sin\beta_a \end{bmatrix} \cdot \\ &\begin{bmatrix} \hat{r} & \hat{t} & \hat{n} \end{bmatrix}^T \end{aligned} \tag{105}$$

Identification of Eqs. [104] and [105] lead to obtaining α_a and β_a as functions of (q_1, q_2, q_3, q_4), ϕ, ξ, Δ_y, and Δ_z:

$$\beta_a = \arcsin T_{a3} \tag{106}$$

$$\sin\alpha_a = \frac{T_{a1}}{\cos\beta_a} \quad \text{and} \quad \cos\alpha_a = \frac{T_{a2}}{\cos\beta_a} \tag{107}$$

V. VTD-NOG & CPD APPLIED TO LUNAR ASCENT

The guidance and control methodology based on the joint use of VTD-NOG and CPD is applied to lunar ascent and orbit injection. The optimal ascent path is derived in a previous section and takes almost 10 minutes.

Further characteristics of the ascent vehicle are the initial mass $m_0 = 4700$ kg, the maximal deflection angles $\bar{\Delta}_y$ and $\bar{\Delta}_z$ (both set to 10 deg), the maximal torque generated by the side jet system $\bar{M}_x$ (set to 2000 N m), the time-varying distance l, and inertia moments I_x, I_y, and I_z,

$$\begin{aligned} l &= l_0 + \dot{l}t \\ I_x = I_{x0} + \dot{I}_x t \quad I_y &= I_{y0} + \dot{I}_y t \quad I_z = I_{z0} + \dot{I}_z t \end{aligned} \tag{108}$$

where

$$l_0 = 1 \text{ m} \qquad \dot{l} = 8.3 \cdot 10^{-4} \text{ m/sec} \tag{109}$$

$$I_{x0} = 4800 \text{ kg m}^2 \qquad \dot{I}_x = -1 \text{ kg m}^2/\text{sec} \tag{110}$$

$$I_{y0} = 9200 \text{ kg m}^2 \qquad \dot{I}_y = -7.5 \text{ kg m}^2/\text{sec} \tag{111}$$

$$I_{z0} = 8100 \text{ kg m}^2 \qquad \dot{I}_z = -8.33 \text{ kg m}^2/\text{sec} \tag{112}$$

These values are similar to those of the ascent module employed in the Apollo 11 mission[30]. The values $\tau_x = \tau_y = \tau_z = 0.1$ sec are picked for the time constants of the actuators.

Moreover, the following values are selected for VTD-NOG & CPD. The sampling interval Δt_S is set to 5 sec, and the CPD gains are determined as follows. First, note that the constant thrust equals $T = n_0 m_0$, the minimum value for l_c is given by l_0, and the maximum values for I_x, I_y, and I_z are respectively I_{x0}, I_{y0}, and I_{z0}. Then, the lower bounds are

$$\underline{G_x} = 1/(2I_{x0}) = 1.04 \cdot 10^{-4} \text{ sec}^{-2} \tag{113}$$

$$\underline{G_y} = Tl_0/(2I_{y0}) = 0.63 \text{ sec}^{-2} \tag{114}$$

$$\underline{G_z} = Tl_0/(2I_{z0}) = 2.79 \text{ sec}^{-2} \tag{115}$$

By inspection of the time behaviors of Φ_c, Θ_c, and Ψ_c in nominal conditions, it seems appropriate picking $\underline{\omega_{nx}} = \underline{\omega_{ny}} = \underline{\omega_{nz}} = 0.7 \text{ sec}^{-1}$, so to obtain an attitude control loop fast enough with respect to the speed of variation of nominal Θ_c, Ψ_c, and of Φ_c, which is identically set to 0. Moreover, proceeding by trial and error $\underline{\zeta_x}$, $\underline{\zeta_y}$, and $\underline{\zeta_z}$ are set to 0.9. Thus, by Eq. [101] and analogous equations for the other PD gains, one obtains $k_{px} = 4700$, $k_{dx} = 6048$, $k_{py} = 0.78$, $k_{dy} = 1.01$, $k_{pz} = 0.69$, and $k_{dz} = 0.89$. In addition, the value 10 Nm is selected for $\bar{M}_{xc}$, whereas the value 1.5 deg is

selected for $\bar{\Delta}_{yc}$ and $\bar{\Delta}_{zc}$, so that the inequalities $|\dot{M}_x| \le 200$ Nm/sec, $|\dot{\Delta}_y| \le 30$ deg/sec, and $|\dot{\Delta}_z| \le 30$ deg/sec are guaranteed (cf. Eq. [95]). Note that Eq. [98] implies that $|\tilde{\Delta}_y|$ is constrained to 1.5 deg. Thus, since $\bar{\Delta}_y = 10$ deg, the same happens to the amplitude of Δ_y (cf. Eq. [84]). The same argument applies to M_x and Δ_z, thus the inequalities $|M_x| \le 10$ Nm and $|\Delta_z| \le 1.5$ deg hold, too. Table I collects the values of all the relevant quantities that must be set in order to apply VTD-NOG & CPD.

Quantity	Value	Unit
Δt_S	5	sec
$\underline{G}_x$	1.04e-4	sec^{-2}
$\underline{G}_x$	0.63	sec^{-2}
$\underline{G}_z$	2.79	sec^{-2}
$\underline{\omega}_{nx}$	0.7	sec^{-1}
$\underline{\omega}_{ny}$	0.7	sec^{-1}
$\underline{\omega}_{nz}$	0.7	sec^{-1}
$\underline{\zeta}_x$	0.9	/
$\underline{\zeta}_y$	0.9	/
$\underline{\zeta}_z$	0.9	/
k_{px}	4700	/
k_{dx}	6048	/
k_{py}	0.78	/
k_{dy}	1.01	/
k_{pz}	0.69	/
k_{dz}	0.89	/
$\bar{M}_{xc}$	10	N
$\bar{\Delta}_{yc}$	1.5	deg
$\bar{\Delta}_{zc}$	1.5	deg

Table I: Parameter settings for VTD-NOG & CPD.

The first reason for the existence of deviations from nominal flight conditions resides in the assumption that the thrust direction points toward the spacecraft longitudinal axis. This alignment condition was assumed for the derivation of the optimal ascent path. However, the actual spacecraft dynamics is driven by a thrust direction not exactly aligned with the longitudinal axis, due to the use of thrust vectoring for attitude control. This circumstance is apparent also by inspection of Fig. VI, which illustrates clearly that the corrected control $\boldsymbol{u}$ does not coincide with the actual control $\boldsymbol{u}_a$, which affects the real dynamics of the center of mass. As a first step, VTD-NOG & CPD has been tested in order to evaluate these deviations, exclusively related to the alignment assumption. The first column of Table I (denoted with NP, standing for "no perturbation") reports the related results (obtained in a single simulation), i.e. the final displacements from the nominal final altitude, declination, and velocity components, and testifies to the excellent accuracy of VTD-NOG & CPD in this context.

However, perturbations can exist that affect the overall spacecraft dynamics. These can be related to the dynamical system itself or to environmental conditions. Monte Carlo (MC) campaigns are usually run, with the intent of obtaining some useful statistical information on the accuracy of the guidance and control algorithm of interest, in the presence of the existing perturbations, which are simulated stochastically.

More specifically, for the initial conditions an error on the initial declination is assumed, with Gaussian distribution, zero mean value and standard deviation $\phi_0^{(\sigma)}$ (for ϕ_0) corresponding to 1 km on the Moon surface. This means that $\phi_0^{(\sigma)} = 0.033$ deg.

A different approach was chosen for the perturbation of the thrust acceleration. In fact, usually the thrust magnitude (and the related acceleration, as a result) exhibits small fluctuations. This time-varying behavior has been modeled through a trigonometric series with random coefficients,

$$n_0^{(p)} = n_0 \left[1 + \sum_{k=1}^{5} \tilde{a}_k \sin\left(\frac{2k\pi t}{t_f^*} \right) + \sum_{k=1}^{5} \tilde{a}_{k+5} \cos\left(\frac{2k\pi t}{t_f^*} \right) \right] \quad [116]$$

where $n_0^{(p)}$ denotes the perturbed value of n_0, whereas the coefficients $\{\tilde{a}_k\}_{k=1,\ldots,10}$ have a random Gaussian distribution centered around the zero and a standard deviation equal to 0.02.

Moreover, also the mass distribution time history may exhibit some unpredictable oscillations, and this is modeled again by means of harmonic terms, for both the the length l, and the inertia moments (I_x, I_y, I_z)

$$l = \dot{l}t + l_0 - \sum_{k=1}^{5} \tilde{c}_k \sin\left(\frac{2k\pi t}{t_f^*} \right) - \sum_{k=1}^{5} \tilde{c}_{k+5} \left[\cos\left(\frac{2k\pi t}{t_f^*} \right) - 1 \right] \quad [117]$$

$$I_x = \dot{I}_x t + I_{x0} + \sum_{k=1}^{5} \tilde{b}_{x,k} \sin\left(\frac{2k\pi t}{t_f^*}\right) + \sum_{k=1}^{5} \tilde{b}_{x,k+5} \left[\cos\left(\frac{2k\pi t}{t_f^*}\right) - 1\right] \quad [118]$$

$$I_y = \dot{I}_y t + I_{y0} + \sum_{k=1}^{5} \tilde{b}_{y,k} \sin\left(\frac{2k\pi t}{t_f^*}\right) + \sum_{k=1}^{5} \tilde{b}_{y,k+5} \left[\cos\left(\frac{2k\pi t}{t_f^*}\right) - 1\right] \quad [119]$$

$$I_z = \dot{I}_z t + I_{z0} + \sum_{k=1}^{5} \tilde{b}_{z,k} \sin\left(\frac{2k\pi t}{t_f^*}\right) + \sum_{k=1}^{5} \tilde{b}_{z,k+5} \left[\cos\left(\frac{2k\pi t}{t_f^*}\right) - 1\right] \quad [120]$$

In Eqs. [117] through [120] the third and fourth terms represent the displacement from the nominal linear time history. The coefficients $\left\{\tilde{b}_{x,k}, \tilde{b}_{y,k}, \tilde{b}_{z,k}, \tilde{c}_k\right\}_{k=1,\ldots,10}$ are random quantities with uniform distribution in proper intervals, such that the perturbed inertia moments $\left(I_x, I_y, I_z\right)$ are nonincreasing in time, while the length l is nondecreasing. It is straightforward to recognize that sufficient conditions for monotonicity are

$$-\frac{l_f - l_0}{20k\pi} \le \tilde{c}_k \le \frac{l_f - l_0}{20k\pi} \quad [121]$$

$$-\frac{I_{j,0} - I_{j,f}}{20k\pi} \le \tilde{b}_{j,k} \le \frac{I_{j,0} - I_{j,f}}{20k\pi} \qquad \left(j = x, y, z\right) \quad [122]$$

where the subscripts 0 and *f* denote the initial and final value of the respective variable.

Furthermore, actuation errors may affect the spacecraft performance. They are modeled through Gaussian noise terms, with zero mean and standard deviation of 0.1 deg; these terms are added to the thrust angles $\tilde{\Lambda}_y$ and $\tilde{\Lambda}_z$ in Eqs. [82] and [83].

Finally, navigation errors exist. They are represented by the displacements between the measured trajectory variables $\left(r, \xi, \phi, v_r, v_t, v_n\right)$ and the actual ones. At each sampling time, these errors are modeled by adding the displacements $\left(\delta r, \delta\xi, \delta\phi, \delta v_r, \delta v_t, \delta v_n\right)$. These perturbing terms are modeled as random Gaussian variables, with zero mean value and time-varying standard deviation given by

$$\sigma_r^{(N)} = \vartheta_1 t \qquad \sigma_\xi^{(N)} = \vartheta_2 t \qquad \sigma_\phi^{(N)} = \vartheta_3 t \quad [123]$$

$$\sigma_{vr}^{(N)} = \vartheta_4 t \qquad \sigma_{vt}^{(N)} = \vartheta_5 t \qquad \sigma_{vn}^{(N)} = \vartheta_6 t \quad [124]$$

where $\vartheta_1 = 0.017$ m/sec, $\vartheta_2 = \vartheta_3 = 1.0 \cdot 10^{-8}$ sec^{-1}, and $\vartheta_4 = \vartheta_5 = \vartheta_6 = 8.7 \cdot 10^{-3}$ m/sec^2. These standard deviations increase in time and have final values $\sigma_{vr,f}^{(N)} = \sigma_{vt,f}^{(N)} = \sigma_{vn,f}^{(N)} = 5$ m/sec, $\sigma_r^{(N)} = 10$ m, and $\sigma_{\xi,f}^{(N)} = \sigma_{\phi,f}^{(N)} = 5.75 \cdot 10^{-6}$.

At the end of VTD-NOG & CPD, two statistical quantities are evaluated, i.e. the mean value and the standard deviation for all of the outputs of interest. The symbols $\overline{\Delta\chi}$ and $\chi^{(\sigma)}$ will denote the mean error (with respect to the nominal value) and standard deviation of χ henceforth.

Two MC campaigns are performed, each including 100 numerical simulations: (i) MC1 assumes all the previously described perturbations, with the exception of navigation errors, whereas (ii) MC2 includes also these. Figs. VIII through XXI refer to MC1 and portray the time histories of the relevant trajectory variables, M_x and its rate, the engine deflection angles and their rates, as well as the commanded and actual attitude angles.

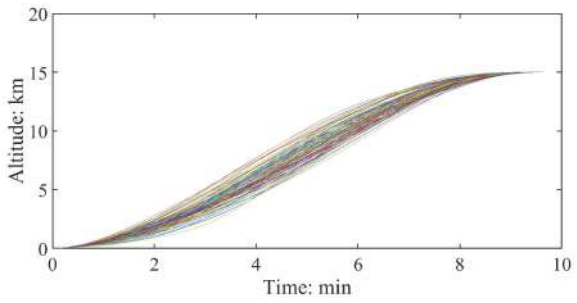

Fig. VIII: Altitude time histories obtained in the MC1 campaign

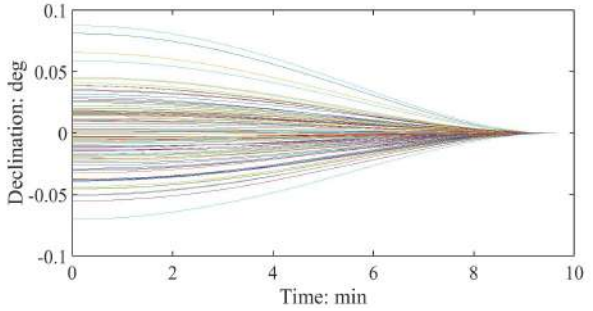

Fig. IX: Declination time histories obtained in the MC1 campaign

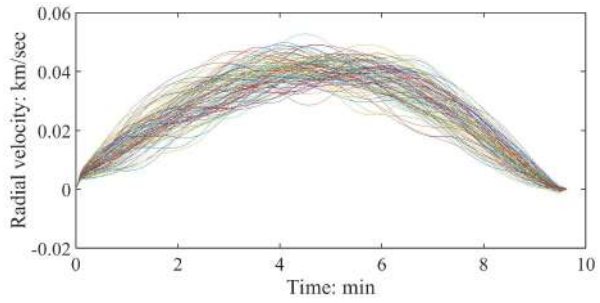

Fig. X: Radial velocity time histories obtained in the MC1 campaign

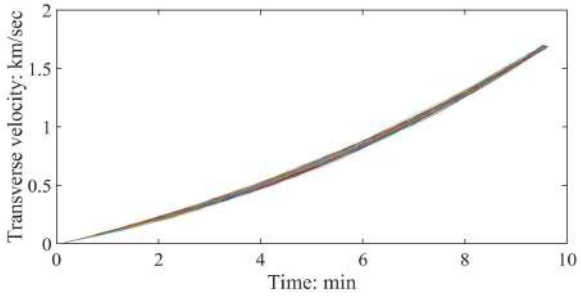

Fig. XI: Transverse velocity time histories obtained in the MC1 campaign

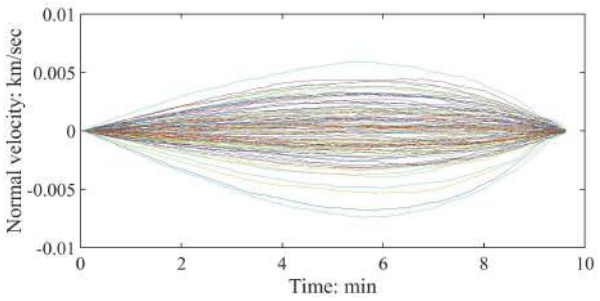

Fig.XII: Normal velocity time histories obtained in the MC1 campaign

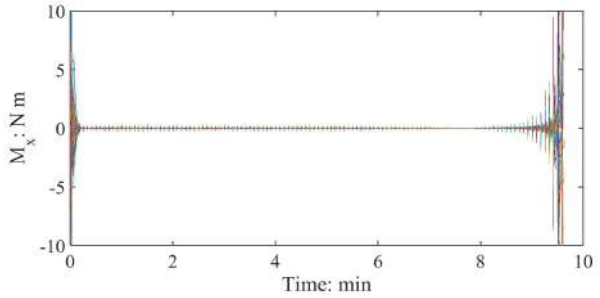

Fig. XIII: Time histories of the torque M_x obtained in the MC1 campaign

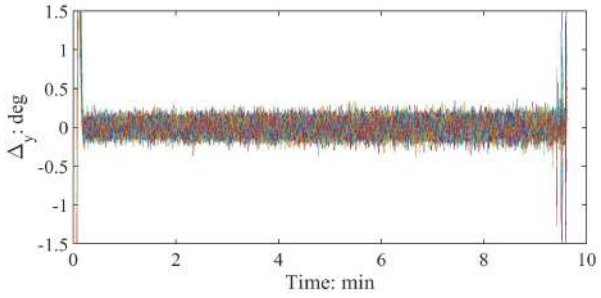

Fig. XIV: Time histories of the engine deflection angle Δ_y obtained in the MC1 campaign

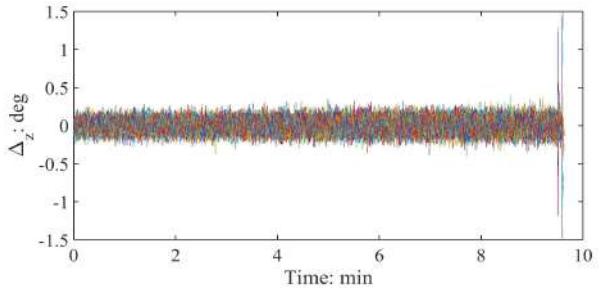

Fig. XV: Time histories of the engine deflection angle Δ_z obtained in the MC1 campaign

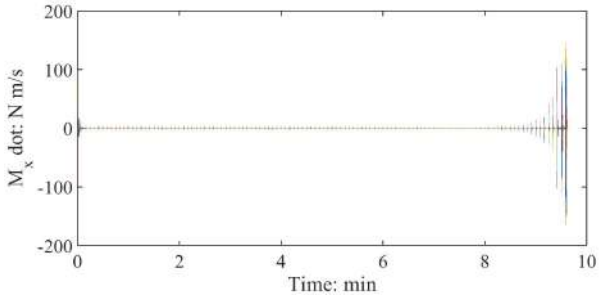

Fig. XVI: Time histories of the torque rate $\dot{M}_x$ obtained in the MC1 campaign

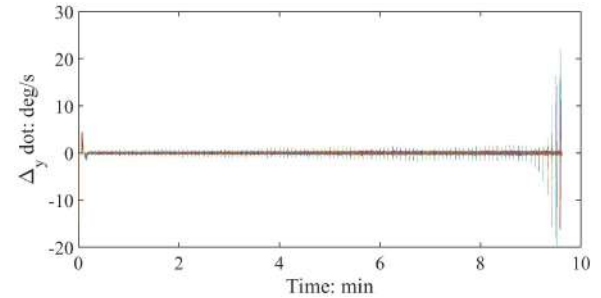

Fig. XVII: Time histories of the engine deflection rate $\dot{\Delta}_y$ obtained in the MC1 campaign

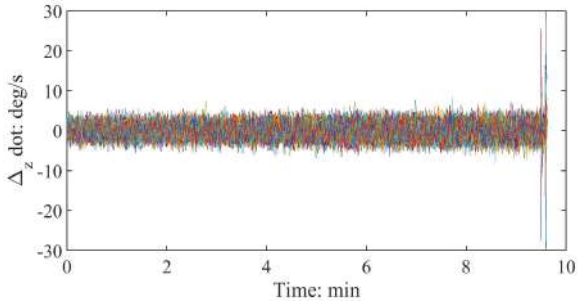

Fig. XVIII: Time histories of the engine deflection rate $\dot{\Delta}_z$ obtained in the MC1 campaign

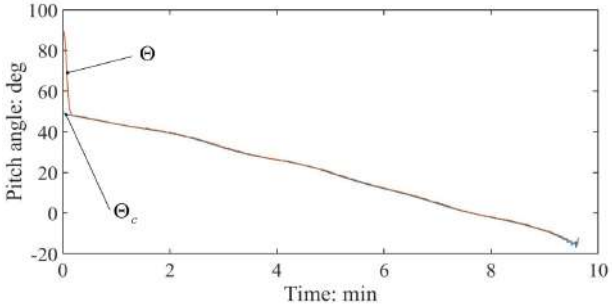

Fig. XIX: Commanded and actual pitch angle obtained in a single MC1 simulation

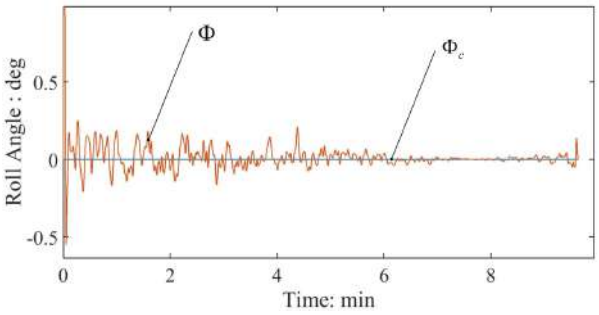

Fig. XX: Commanded and actual roll angle obtained in a single MC1 simulation

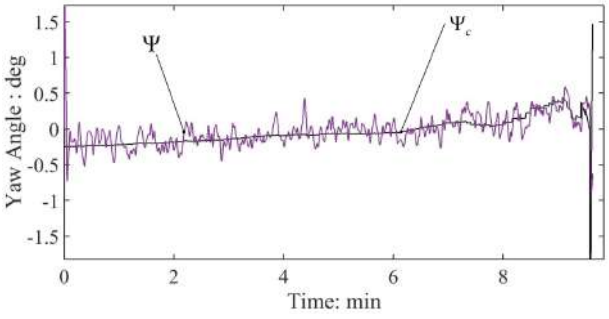

Fig. XXI: Commanded and actual yaw angle obtained in a single MC1 simulation

Moreover, Table II reports the statistics on the errors at injection and the time of flight. Inspection of this table reveals that VTD-NOG & CPD guarantees orbit injection with excellent accuracy, despite the relatively relaxed sampling time. However, comparison of the results obtained in MC1 and MC2 points out that navigations errors are responsible of a noticeable increase on the standard deviations of some errors (e.g., that on the final radius), while the average final values are very satisfactory both for MC1 and for MC2. Furthermore, the average time of flight is very close to the nominal value, and the corresponding standard deviation is modest.

As a final remark, the runtime of VTD-NOG & CPD on an Intel i5-3570K @ 3.40 GHz takes 6.04 min (while the nominal time of flight exceeds 9 min), and this guarantees that the guidance and control algorithm at hand can be implemented in real time.

Statistics	NP	MC1	MC2
$\overline{\Delta r_f}$ (m)	8.8e-3	0.33	1.96
$\overline{\Delta \phi_f}$ (deg)	0	-3.1e-7	6.2e-5
$\overline{\Delta v_{rf}}$ (m/sec)	-0.20	-0.14	0.64
$\overline{\Delta v_{tf}}$ (m/sec)	-2.64	-2.67	-7.03
$\overline{\Delta v_{nf}}$ (m/sec)	0	0.01	-0.26
$\overline{t_f}$ (min)	9.58	9.57	9.58
$r_f^{(\sigma)}$ (m)	/	0.80	36.0
$\phi_f^{(\sigma)}$ (deg)	/	8.7e-6	1.2e-3
$v_{rf}^{(\sigma)}$ (m/sec)	/	0.36	7.34
$v_{tf}^{(\sigma)}$ (m/sec)	/	5.46	6.87
$v_{nf}^{(\sigma)}$ (m/sec)	/	0.14	7.37
$t_f^{(\sigma)}$ (min)	/	0.03	0.03

Table II: Statistics on the errors on the final state and on the time of flight

VI. CONCLUDING REMARKS

This work proposes VTD-NOG & CPD, a new, general-purpose guidance and control algorithm for space vehicles, and describes its application to three-dimensional lunar ascent and orbit injection. VTD-NOG is a feedback guidance technique based upon minimizing the second differential of the objective function along the perturbed trajectory. This minimization principle leads to deriving all the corrective maneuvers. Due to adoption of a normalized time scale as the domain in which the nominal trajectory is defined, the gain matrices remain finite for the entire

time of flight, while the updating law for the time of flight and the termination criterion find consistent definitions. VTD-NOG identifies the trajectory corrections by assuming a thrust direction always aligned with the longitudinal axis of the spacecraft. CPD is employed for attitude control through TVC and SJS, and pursues this alignment condition. Unlike standard PD schemes, CPD introduces an appropriate saturation action, with the aim of maintaining the rate of the engine deflection angles within acceptable limits. This new guidance and control concept is applied to lunar ascent and orbit injection, with the intent of testing its capabilities. Oscillating perturbations of the propulsive thrust, incorrect initial position, actuation and navigation errors, and imperfect modeling of the mass distribution and variation have been considered. They yield perturbed three-dimensional ascent paths. This implies that the attitude motion is triaxial, because yaw, roll, and pitch dynamics are involved while pursuing the thrust direction corrections. In order to address this issue, the attitude control algorithm is designed in a general and effective way, with the final aim of determining the actual thrust vector direction. Extensive Monte Carlo simulations point out that orbit injection occurs with excellent accuracy, thus demonstrating that VTD-NOG & CPD indeed represents an effective methodology for the application at hand. Due to its generality, VTD-NOG & CPD may be regarded as a promising approach for guidance and control of space vehicles employed in a wide variety of mission scenarios.

VII. ACKNOWLEDGEMENT

The authors wish to express their gratitude to Giovanni Palmerini for his help.

APPENDIX A. EQUATIONS OF MOTION

The three-dimensional equations of motion that govern the dynamics of the spacecraft center of mass regard its position and velocity.

With reference to Fig. I(a), in the inertial frame $\left(\hat{c}_1,\hat{c}_2,\hat{c}_3\right)$ the position vector $\boldsymbol{r}$ can be expressed as a function of radius r, right ascension ξ, and declination ϕ,

$$\boldsymbol{r} = r\left[\cos\xi\cos\phi \quad \sin\xi\cos\phi \quad \sin\phi\right]\left[\hat{c}_1 \quad \hat{c}_2 \quad \hat{c}_3\right]^T \quad [125]$$

whereas the velocity vector $\boldsymbol{v}$ can be written in terms of its components $\left(v_r,v_t,v_n\right)$ along the local horizontal (rotating) frame $\left(\hat{r},\hat{t},\hat{n}\right)$ (termed LH-frame, cf. Fig. I(a)):

$$\boldsymbol{v} = \left[v_r \quad v_t \quad v_n\right]\left[\hat{r} \quad \hat{t} \quad \hat{n}\right]^T \quad [126]$$

Let μ, $\tilde{m}$, and $\boldsymbol{T}$ denote respectively the gravitational parameter of the attracting body, the spacecraft mass, and its propulsive thrust. Under the assumption of considering only the dominating term of the gravitational force, the kinematics and dynamics (vector) equations involve respectively the time derivative of $\boldsymbol{r}$ and $\boldsymbol{v}$, and are

$$\frac{d\boldsymbol{r}}{dt} = \boldsymbol{v} \quad [127]$$

$$\frac{d\boldsymbol{v}}{dt} = -\frac{\mu}{r^3}\boldsymbol{r} + \frac{\boldsymbol{T}}{\tilde{m}} \quad [128]$$

These equations yield the scalar differential equations for the state variables $\left(r,\xi,\phi,v_r,v_t,v_n\right)$, through the developments that follow.

As a first step, the LH-frame is obtained through a sequence of two elementary rotations: first counterclockwise rotation about axis 3 by angle ξ, and second clockwise rotation about axis 2 by angle ϕ:

$$\begin{aligned}\left[\hat{r} \quad \hat{t} \quad \hat{n}\right]^T &= \mathbf{R}_2\left(-\phi\right)\left[\hat{\imath} \quad \hat{\jmath} \quad \hat{k}\right]^T \\ &= \mathbf{R}_2\left(-\phi\right)\mathbf{R}_3\left(\xi\right)\left[\hat{c}_1 \quad \hat{c}_2 \quad \hat{c}_3\right]^T\end{aligned} \quad [129]$$

The angular rate of the LH-frame with respect to the inertial frame is

$$\boldsymbol{\omega} = \dot{\xi}\hat{c}_3 - \dot{\phi}\hat{\jmath} \quad [130]$$

Combination of Eqs. [129] and [130] leads to

$$\boldsymbol{\omega} = \left[\dot{\xi}\sin\phi \quad -\dot{\phi} \quad \dot{\xi}\cos\phi\right]\left[\hat{r} \quad \hat{t} \quad \hat{n}\right]^T \quad [131]$$

Then, using the Poisson's formula, the left-hand side of Eq. [127] may be written as

$$\frac{d\boldsymbol{r}}{dt} = \dot{r}\hat{r} + \boldsymbol{\omega}\times\boldsymbol{r} = \left[\dot{r} \quad r\dot{\xi}\cos\phi \quad r\dot{\phi}\right]\left[\hat{r} \quad \hat{t} \quad \hat{n}\right]^T \quad [132]$$

whereas the right-hand side is given by Eq. [126]. Combining Eqs. [126] and [132] leads to Eqs. [4]-[6]. Moreover, using the Poisson's formula again, the left-hand side of Eq. [128] is

$$\frac{d\boldsymbol{v}}{dt} = \dot{v}_r\hat{r} + \dot{v}_t\hat{t} + \dot{v}_n\hat{n} + \boldsymbol{\omega}\times\boldsymbol{v} \quad [133]$$

Using also Eqs. [4]-[6], the previous relation yields

$$\frac{d\boldsymbol{v}}{dt} = \begin{bmatrix} \dot{v}_r - \dfrac{v_t^2 + v_n^2}{r} \\ \dot{v}_t + \dfrac{v_r v_t - v_n v_t\tan\phi}{r} \\ \dot{v}_n + \dfrac{v_r v_n + v_t^2\tan\phi}{r} \end{bmatrix}^T \begin{bmatrix}\hat{r}\\ \hat{t}\\ \hat{n}\end{bmatrix} \quad [134]$$

Due to the geometric definition of α and β (cf. Fig. I(b)), the right-hand side of Eq. [128] is

$$-\frac{\mu}{r^3}\boldsymbol{r}+\frac{\boldsymbol{T}}{m}=\begin{bmatrix} -\frac{\mu}{r^2}+\frac{T}{\tilde{m}}\cos\beta\sin\alpha \\ \frac{T}{\tilde{m}}\cos\beta\cos\alpha \\ \frac{T}{\tilde{m}}\sin\beta \end{bmatrix}^T \begin{bmatrix} \hat{r} \\ \hat{t} \\ \hat{n} \end{bmatrix} \quad [135]$$

Combining Eqs. [134] and [135] finally leads to Eqs. [7] -[9].

REFERENCES

[1] D. K. Geller, "Linear Covariance Techniques for Orbital Rendezvous Analysis and Autonomous Onboard Mission Planning," *Journal of Guidance, Control, and Dynamics*, Vol. 29, No. 6, pp. 1404—1414, 2006

[2] A. Marcos, L. F. Peñín, J. Sommer, and E. Bornschlegl, "Guidance and Control Design for the Ascent Phase of the Hopper RLV," AIAA Guidance, Navigation and Control Conference and Exhibit, Honolulu, HI, 2008. AIAA Paper 2008-7125

[3] Q. M. Lam, M. B. McFarland, M. Ruth, D. Drake, D. B. Ridgely, and M. W. Oppenheimer, "Adaptive Guidance and Control for Space Access Vehicle Subject to Control Surface Failures," AIAA Guidance, Navigation and Control Conference and Exhibit, Honolulu, HI, 2008. AIAA Paper 2008-7163

[4] B. Tian, W. Fan, and Q. Zong, "Integrated guidance and control for reusable launch vehicle in reentry phase," *Nonlinear Dynamics*, Vol. 80, No. 1-2, pp. 397—412, 2015

[5] F.-K. Yeh, "Sliding-mode-based contour-following controller for guidance and autopilot systems of launch vehicles," *Proceedings of the Institution of Mechanical Engineers, Part G: Journal of Aerospace Engineering*, Vol. 227, No. 2, pp. 285—302, 2015

[6] P. Lu, "Optimal Feedback Control Laws Using Nonlinear Programming," *Journal of Optimization Theory and Applications*, Vol. 71, No. 3, pp. 599—611, 1991

[7] B. Kugelmann and H. J. Pesch, "New General Guidance Method in Constrained Optimal Control, Part 1: Numerical Method," *Journal of Optimization Theory and Applications*, Vol. 67, No. 3, pp. 421—435, 1990

[8] B. Kugelmann and H. J. Pesch, "New General Guidance Method in Constrained Optimal Control, Part 2: Application to Space Shuttle Guidance," *Journal of Optimization Theory and Applications*, Vol. 67, No. 3, pp. 437—446, 1990

[9] H. H. Afshari, A. B. Novinzadeh, and J. Roshanian, "Determination of Nonlinear Optimal Feedback Law for Satellite Injection Problem Using Neighboring Optimal Control," *American Journal of Applied Sciences*, Vol. 6, No. 3, pp. 430—438, 2009

[10] H. Seywald and E. M. Cliff, "Neighboring Optimal Control Based Feedback Law for the Advanced Launch System," *Journal of Guidance, Control, and Dynamics*, Vol. 17, No. 3, pp. 1154—1162, 1994

[11] H. Yan, F. Fahroo, and I. M. Ross, "Real-Time Computation of Neighboring Optimal Control Laws," AIAA Guidance, Navigation and Control Conference and Exhibit, Monterey, CA, 2002. AIAA Paper 2002-4657

[12] C. B. Charalambous, S. N. Naidu, and J. L. Hibey, "Neighboring Optimal Trajectories for Aeroassisted Orbital Transfer Under Uncertainties," *Journal of Guidance, Control, and Dynamics*, Vol. 18, No. 3, pp. 478—485, 1995

[13] D. G. Hull, *Optimal Control Theory for Applications*, Springer International Edition, New York, NY, pp. 199—254, 2003

[14] D. G. Hull and M. J. Nowak, "Neighboring Suboptimal Control for Vehicle Guidance," AAS/AIAA Space Flight Conference, Pasadena, CA, 1993. Paper AAS 93-151

[15] A. Tewari, *Advanced Control of Aircraft, Spacecraft and Rockets*, Wiley, Chichester, UK, ch. 5, 2011

[16] A. L. Greensite, *Analysis and design of space vehicle flight control systems. Control theory: Volume II*, Spartan Books, New York, pp. 175—192, 1970

[17] M. Pontani and F. Celani, "Lunar Ascent and orbit Injection via Neighboring Optimal Guidance and Constrained Attitude Control," *Journal of Aerospace Engineering*, Vol. 31, No. 5, 2018

[18] M. Pontani and F. Celani, "New Implicit Neighboring Optimal Guidance and Attitude Control for Three-Dimensional Lunar Ascent," Proceedings of the 68th International Astronautical Congress, Adelaide, Australia, 2017. Paper IAC-17-C1.4.8

[19] M. Pontani and B. A. Conway, "Particle Swarm Optimization Applied to Space Trajectories," *Journal of Guidance, Control and Dynamics*, Vol. 33, No. 5, pp. 1429–1441, 2010

[20] M. Pontani, P. Ghosh, and B. A. Conway, "Particle Swarm Optimization of Multiple-Burn Rendezvous Trajectories," *Journal of Guidance, Control, and Dynamics*, Vol. 35, No. 4, 2012, pp. 1192–1207

[21] M. Pontani and B. A. Conway, "Optimal Low-Thrust Orbital Maneuvers via Indirect Swarming Method," *Journal of Optimization Theory and Applications*, Vol. 162, No. 1, pp. 272—292, 2014

[22] M. Pontani and B. A. Conway, "Optimal Finite-Thrust Rendezvous Trajectories Found via Particle Swarm Algorithm," *Journal of Spacecraft and Rockets*, Vol. 50, pp. 1222—1234, 2013

[23] M. Pontani and B. A. Conway, "Particle Swarm Optimization Applied to Impulsive Orbital Transfers," *Acta Astronautica*, Vol. 74, pp. 141—155, 2012

[24] M. Pontani, G. Cecchetti, and P. Teofilatto, "Variable-Time-Domain Neighboring Optimal Guidance, Part 1: Algorithm Structure," *Journal of Optimization Theory and Applications*, Vol. 166, No. 1, pp. 76—92, 2016
[25] M. Pontani, G. Cecchetti, and P. Teofilatto, "Variable-time-domain neighboring optimal guidance applied to space trajectories," *Acta Astronautica*, Vol. 115, pp. 102—120, 2015
[26] W. Du and B. Wie, "Ascent Flight Control of Ares-I Crew Launch Vehicle in the Event of Uncontrolled Roll Drift," AIAA Guidance, Navigation, and Control Conference, Chicago, IL, 2009.
[27] H. Schaub and J. L. Junkins, *Analytical Mechanics of Space Systems*, AIAA Education Series, Reston, VA, pp. 95-97, 206-209, 2003
[28] F. L. Markley and J. L. Crassidis, *Fundamentals of Spacecraft Attitude Determination and Control,* Springer, New York, p. 289, 2014.
[29] H. K. Khalil, *Nonlinear Sytems*, Prentice Hall, Upper Saddle River, NJ, pp. 102–103, 2000.
[30] R. Godwin, *Apollo 11 – The NASA Mission Reports Volume 3*, Apogee Books, p. 215, 2002